Check for updates

AGU ADVANCING EARTH AND SPACE SCIENCE

Water Resources Research

RESEARCH ARTICLE
10.1029/2021WR029584

Effect of Poroelastic Coupling and Fracture Dynamics on Solute Transport and Geomechanical Stability

Minh Tran[1] and Birendra Jha[1]

[1]Mork Family Department of Chemical Engineering & Materials Science, University of Southern California, Los Angeles, CA, USA

Key Points:

- Quantitative characterization of the geomechanical coupling effect on transport metrics: solute breakthrough time and degree of mixing
- Mechanistic understanding of permeability evolution and fracture stability during hydrodynamically unstable transport
- Effect of the injected-to-resident fluid viscosity ratio on the stress state and fracture stability

Supporting Information:

Supporting Information may be found in the online version of this article.

Correspondence to:

B. Jha,
bjha@usc.edu

Citation:

Tran, M., & Jha, B. (2021). Effect of poroelastic coupling and fracture dynamics on solute transport and geomechanical stability. *Water Resources Research*, *57*, e2021WR029584. https://doi.org/10.1029/2021WR029584

Received 26 JAN 2021
Accepted 19 SEP 2021

© 2021. American Geophysical Union. All Rights Reserved.

Abstract The coupling between solute transport and rock's geomechanical processes, for example, flow-induced fracture activation, has emerged as an important hydrogeological challenge due to its role in applications such as underground waste disposal, carbon sequestration, contaminant remediation, enhanced oil recovery, and tracer-based reservoir surveillance. Despite recent advances in modeling flow and geomechanics coupling, a holistic approach to capturing the synergy between fluid flow, solute transport, induced stresses, and fracture mechanics is lacking. This study investigates the rich interplay between these processes within a novel computational framework that is proposed to solve the coupled flow, transport, geomechanics, and fracture mechanics problem. The Embedded Discrete Fracture Modeling (EDFM) method is used to model the flow and transport processes in fractured porous media while an improved Bandis model is employed to capture the fracture mechanical response to flow-induced stress perturbations. The role of transport-geomechanics coupling in modulating the spreading and miscibility of a solute slug during viscously unstable flows is examined. We investigate how flow-transport coupling, parameterized through the solute viscosity contrast and the fracture permeability, influences the stress state and fracture stability in the domain. A case study, inspired by a huff-n-puff tracer flowback study, is conducted to investigate the applicability of the proposed framework in the field. A sensitivity analysis is performed to evaluate the dependence of global transport characteristics, permeability evolution, and fracture stability on parameters dictating the strength of coupling between geomechanics, flow, and transport.

1. Introduction

Injection of fluids into naturally or hydraulically fractured formations has been an important research topic due to its relevance in a vast number of engineering applications: waste disposal (Cornaton et al., 2008; McCarthy & Zachara, 1989; Witherspoon et al., 1981), carbon sequestration (Iding & Ringrose, 2010), contaminant transport (Sahimi, 2011), enhanced oil recovery (Jiménez-Martínez et al., 2016), and tracer surveillance (Hu & Moran, 2005; Rugh & Burbey, 2008; Warner et al., 2014). In many applications, a key objective of the numerical model built to simulate the processes is to quantify the mixing between the injected and resident fluids and quantify the extent of the associated mixing zone (Bonazzi et al., 2020, 2021; Cirpka & Valocchi, 2007; Dentz et al., 2011; Jha et al., 2011a; Z. Zhao et al., 2011). In cyclic well operations, where the well alternates or cycles through injection and production/withdrawal stages, the evolution of fluid mixing is complicated by short time scale variations in the pore pressure field. Often, the reservoir of interest is geomechanically sensitive and deformable due to the presence of pre-existing fractures, unconsolidated formations, or excessive flow-induced stresses. Resolving the geomechanical coupling effect in those reservoirs becomes critically dependent on modeling the effect of stress-modulated processes such as fracture opening and shear failure on mass transport processes such as advection and diffusion (Fox et al., 2011; Latham et al., 2013; Matthäi et al., 2010; Tran & Jha, 2020; Yan et al., 2019). This is required to answer questions such as how much change in the breakthrough time or degree of mixing corresponds to a given change in the average volumetric stress during groundwater withdrawal.

The presence of hydraulically stimulated and natural fractures in a low permeability rock adds an extra dimension of complexity because the characteristic length and time scales of flow and deformation processes can be markedly different between the fracture and the host rock domains. Often understood as displacement discontinuities, fractures have been proven to make a first-order impact on the flow behavior of any rock (Hardebol et al., 2015; Levison & Novakowski, 2012) by altering its permeability. While accounting for

all individual fractures in a reservoir is computationally intractable and unnecessary, the contribution of a subset of fractures, at length scales relevant to the dominant physical processes in the problem, must be assessed. The role of flow-geomechanical coupling in modulating hydraulic properties such as stress-dependent permeability and porosity is increasingly recognized as a necessity in reservoir-scale simulation models (Bubshait & Jha, 2019; Rutqvist & Stephansson, 2003; Meguerdijian & Jha, 2021). Flow processes can also change the spatial and temporal evolution of stress state and fracture dynamics, which affect the mechanical stability of fractures and formation integrity (Jin & Zoback, 2018). Therefore, a tightly coupled flow and geomechanics computational framework (Tran & Jha, 2020; X. Zhao & Jha, 2019, 2021) is often required to correctly encapsulate and explain the interaction among these underlying processes. This can help us find geomechanical signals, for example, change in the magnitude and direction of principal stresses or activation/healing of fractures oriented along a certain direction, that we can monitor in the field to infer the plume size and dilution during injection.

Modeling of discontinuities such as fractures usually falls under two popular categories of methods: discrete fracture network modeling and continuum modeling (such as the continuum damage mechanics approach [Bubshait & Jha, 2019; Pogacnik et al., 2016; Yan et al., 2019]). Methods in each category have their own merits and drawbacks, most of which can be understood in terms of a method's sensitivity to mesh size dependency, the capability to model localization of flow or deformation and the resulting anisotropic response, and the computational cost to achieve a certain order of numerical accuracy. The cost, which is related to the number of iterations required to solve the discretized linearized system, is often expressed in terms of the number of degrees of freedom and/or the condition number of the Jacobian matrix of the discrete system. The EDFM approach capitalizes on the best features of discrete and continuum approaches to model the effect of fractures while maintaining a relatively lower cost. The basic idea of EDFM is to represent fractures using a structured gridding scheme, separate from the host matrix grid, and use special non-neighboring connections to model the fluxes between fracture and matrix (Hajibeygi et al., 2011; Lee et al., 2001). EDFM allows a numerically fast and stable representation of individual fractures' contribution to flow and transport processes. Compared to traditional fracture modeling methods such as dual-continuum modeling, local grid refinement, and unstructured gridding, EDFM offers a balance between accuracy, flexibility, gridding, and computational efficiency. To improve cross-media flux transfer in media with high conductivity contrasts, for example, in hydraulically fractured shales or geothermal rocks, Tene et al. (2017) proposed pEDFM with adjustments of matrix-matrix and fracture-matrix transmissibilities in the immediate surrounding of the explicit fractures. Compartmental EDFM (c-EDFM) allows sub-grid resolution by splitting the matrix grid when a fracture grid intersects a matrix cell (Chai et al., 2018). Sangnimnuan et al. (2018) developed a coupled flow-geomechanics model with EDFM to characterize stress evolution during fluid production from ultralow permeability reservoirs and to model stress redistribution and reorientation induced by the depletion. Norbeck et al. (2016) addresses how to include nonlinear evolution of nucleated tensile fracture and shear failure events. Moinfar et al. (2013) models the change in aperture and associated permeability of an evolving fracture network via the effective normal stresses acting on fracture planes within an EDFM framework.

Despite a recent shift of focus to coupled flow-geomechanical modeling, there have been limited attempts to model transport phenomena in a complex fracture network under the framework of poroelasticity. The effect of geomechanical coupling on solute spreading, mixing, and viscous fingering in stress-sensitive reservoirs has been explored recently (Sweeney & Hyman, 2020; Tran & Jha, 2020; Tran et al., 2018). In addition, recent advances in understanding fracture dynamics have shed new light on inherently strong nonlinearities that exist between the state of stress and closure and dilation of natural joints (X. Li et al., 2020; Olsson & Barton, 2001). Often, these nonlinearities lead to hysteresis in the mechanical response of the jointed rock when subjected to loading/unloading cycles over time scales of interest. Hysteresis in stress-strain behavior, post-peak shear strength, shear induced dilation are required to improve fracture modeling in aquifers deforming under injection/production (Asadollahi & Tonon, 2010). Yet, many modern-day geomechanical simulators neglect this behavior because of the lack of a computationally efficient poroelastic model for fractured rocks. This paper attempts to bridge these technical gaps by proposing modifications in the classical Bandis model (Bandis et al., 1983), implementing it within a coupled flow-transport-poroelastic framework, and successfully demonstrating its capability in predicting the following observables

Table 1
Groundwater Chemicals With Viscosity μ_1 Different From the Water Viscosity μ_0

Chemical	Viscosity (cp)	$R = \ln \frac{\mu_0}{\mu_1}$
Benzene	0.6	0.39
Toluene	0.56	0.46
Ethylbenzene	0.64	0.33
O-Xylene	0.76	0.16
Trichloroethylene (TCE)	0.55	0.48
No. 4 fuel oil	36	−3.7
Trans-1,2dichloroethylene	0.4	0.8
Chlorobenzene	0.8	0.11
m-Cresol (pesticides, antiseptics)	6.1	−1.92
Diesel	2.2	−0.9
MTBE (gasoline additive)	0.37	0.88
Propane	0.1	2.19

Note. A water viscosity of 0.89 cp at 25°C is assumed.

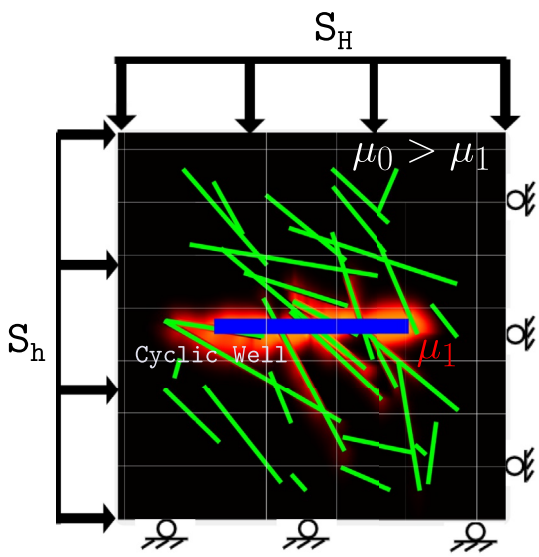

Figure 1. A physical model of tracer injection, tracer soaking or chase fluid injection, and tracer-water withdrawal in a reservoir populated with discrete natural fractures of different lengths and orientations. The horizontal well is intersected by some of the fractures. The initial state of stress in the reservoir is determined by boundary compressions S_h and S_H and zero normal displacement roller boundary conditions. The fractures are denoted by the green lines. The cyclic well is denoted by the thick blue line. The yellow-shaded region around the well indicates the mixture of injected tracer (viscosity μ_1) and resident water (viscosity μ_0), which forms a short time after tracer injection begins at the well. The remaining black domain is saturated with the resident fluid.

during tracer tests in aquifers with complex fracture networks: the tracer breakthrough profile, pore pressure field, and aquifer stress and strain fields around the well.

The physical properties of a solute, which can be a contaminant or a remediation agent, can vary in space and time due to the dependence of solute density, viscosity, or diffusivity on the concentrations of the dissolved species (Flowers & Hunt, 2007). Further, the contaminant viscosity may change with time due to phase separation, dissolution, and evaporation of lighter volatile components (Mercer & Cohen, 1990). Contaminant remediation processes often alter the dynamic properties of contaminant plumes. More specifically, remediation by injection of steam, surfactants, oxidizing agents, or polymer can produce a mobile, dissolved-phase plume with a viscosity that is different from the viscosity of the fluid bank ahead or behind it. Table 1 displays the viscosity and log viscosity ratio R of some groundwater chemicals compared to water. Even for non-aqueous phase liquid (NAPL) contaminants, which are considered mostly immiscible with water, miscible plumes are created as components partition from the NAPL phase into the flowing groundwater (Poulsen & Kueper, 1992). This has two major implications for contaminant transport. First, changes in the viscosity can affect contaminant mobility even in homogeneous permeability fields. Second, when a less viscous fluid is displacing a more viscous fluid, the transport becomes hydrodynamically unstable and culminates into viscous fingering (Homsy, 1987), which leads to stretching of the plume interface and enhanced mixing (Jha et al., 2011b; Nicolaides et al., 2015), which then affects contaminant recovery. To answer questions such as whether solute fingering leads to more dilution in a stiffer rock with fracture activation or in a softer, intact rock with large porosity changes, we need to understand the role of transport-geomechanics coupling in advection-dominated transports.

Below we present our modeling framework in the context of a push-chase-pull tracer test and use the model to elucidate physical mechanisms that arise solely due to the two-way coupling between flow, transport, and poroelasticity. The novelty of our work lies in unraveling these coupling mechanisms and exploring their relationships during hydrodynamically unstable transports in fractured porous media. In particular, we focus on the mechanisms that affect the mixing and spreading of the injected tracer, because these processes control the effectiveness of contaminant removal/remediation in groundwater applications. Finally, we use the framework to analyze the sensitivity of the field observables to changes in various rock-fluid properties, which is essential for applying the proposed framework to subsurface problems where properties may vary over large and/or uncertain ranges.

2. Physical Model

We consider a horizontal section of an aquifer with a horizontal well in the middle (Figure 1) that injects and produces alternatingly. The reservoir is fully saturated with a single-phase fluid (water) and is under hydromechanical equilibrium with external stresses S_h and S_H, which are the minimum and maximum principal horizontal compressions, respectively, from regional tectonics. The stochastic fracture network depicted there is inspired by a tracer flowback study (J. Li et al., 2016) and is generated using the FracGen simulator based on fracture density, formation

resistivity-based imaging logs, and the tracer breakthrough curve (J. Li et al., 2016; Myshakin et al., 2015). This fracture network is designed to encompass complexities such as fracture-to-fracture intersections, well-to-fracture crossings, and heterogeneity in fracture orientation with respect to the S_H direction. The cyclic well first acts as an injector, injecting a slug of tracer that is perfectly miscible with the in situ fluid but has a lower viscosity. The top and bottom boundaries are open to drainage at a fixed pressure that is lower than the initial aquifer pore pressure. As the less viscous slug moves through the aquifer and displaces the more viscous in situ fluid, the Saffman-Taylor hydrodynamic instability initiates at the tracer front giving rise to viscous fingering. The strength of fingering depends on the viscosity contrast between tracer and water, the tracer injection rate, tracer diffusivity, and the characteristics of permeability field (Tran & Jha, 2020), which in this model is dominated by the fracture network. We stop the injection of tracer when it breaks through at either of the two boundaries. Following breakthrough, the well switches to injection of the in-situ fluid (zero tracer concentration) to push the tracer further into the aquifer, and we call this duration the tracer soaking period. The soaking period lasts 30 days and is followed by the tracer extraction or withdrawal period, which is 90 days in the model. During withdrawal, the well produces both the tracer and the in-situ water. This process resembles either a typical huff-n-puff operation in enhanced oil recovery (EOR) or a push-and-pull tracer test in groundwater surveillance. In those applications, the observed pressure change during the injection period is often in the range of 10–30 MPa (J. Li et al., 2016).

The physical model is designed to investigate coupling between geomechanics and transport in fractured porous media during both injection and withdrawal episodes. Since the pore pressure is coupled to both the tracer velocity and the effective stress, we can use this model to probe the coupling between transport and deformation processes to extract possible physical mechanisms arising from such coupling. This will allow us to address questions such as how poroelasticity affects the mixing and spreading of solute transport and how flow-transport coupling, manifested through viscous fingering, impacts stress state and fracture stability. We use the same model to examine how stress changes dictate permeability evolution and how transport metrics are modulated by fracture mechanics.

We make the following assumptions, which are appropriate for the physical problem at hand: (a) slightly compressible fluid, (b) small strain, (c) quasi-static equilibrium, (d) linear elasticity, (e) single-phase flow, (f) isotropic material behavior, (g) isothermal system, and (h) first contact miscibility between the fluids. Given our focus on groundwater transport problems with low values of induced stresses compared to, for example, hydraulic fracturing problems, we make additional assumptions regarding the fracture behavior: (i) mechanical equilibrium in the domain is governed by the deformation of matrix only, and the fracture deformation is limited to stress-dependent changes in the fracture aperture, (j) the gradient of fracture pore pressure normal to the fracture is negligible. Assumption (i) suggests that volumetric strain occurs only in the host matrix and not in the fractures. Thus, the fracture pressure is coupled only to the matrix pressure perturbation and not coupled directly to the mechanical deformation of the matrix. Input parameters such as the well injection rate and the matrix permeability are selected such that the likelihood of fracture propagation or nucleation is negligible. Therefore, in this study, dynamic propagation of fracture is not considered and stress-dependent changes in fracture aperture are modeled via constitutive equations such as the Bandis model (Bandis et al., 1983). As the fractures are generally very thin and highly permeable compared to the surrounding host rock, assumption (j) is generally valid.

3. Mathematical Model

We consider single-phase flow and tracer transport through a poroelastic and deformable solid in two dimensions. Below, we present the governing equations in the strong form for both fracture and matrix domains. The equations will be converted into the respective weak forms and discretized. We adopt a continuum representation of a macroscopic model of the poroelastic medium, where fluid and solid are viewed as overlapping continua (Coussy, 2004). Equations of quasi-static equilibrium, solid and fluid mass conservation, and advective-diffusive transport govern the system's behavior in space and time under the imposed initial and boundary conditions as well as the applicable constitutive laws for the solid, fluid, and tracer components. We will cast the problem into a formulation where the primary unknowns are as follows: the excess pressure in the matrix domain, the excess pressure in the fracture domain, the excess displacement in the matrix, the normalized concentration of tracer in the matrix, and the normalized concentration of

tracer in the fracture domain. Here, "excess" is defined as the difference between a quantity's current value and its reference value; see Section 3.6.

3.1. Fluid Mass Conservation

The 2D model in the Cartesian domain has an area $\Omega = (L_x \times L_y)$, where L_x and L_y are the dimensions in the x and y directions. We denote the closed boundary of the domain by Γ. The initial matrix porosity is ϕ_0, and the matrix permeability k^m is assumed to be isotropic and constant in time. Subscript 0 indicates the initial condition and superscripts m, w and f denote matrix, well, and fracture domains respectively. The initial fracture permeability k_0^f is the same for all fractures so that the dependence of permeability on stress can be compared easily. The domain is saturated with a fluid of density ρ_f, compressibility C_f, and viscosity μ_f. The fluid mass conservation equations for single-phase slightly compressible flow under infinitesimal deformation in the matrix and fracture domains are

$$\frac{1}{M^m}\frac{\partial p^m}{\partial t} + \alpha^m \frac{\partial \epsilon_v}{\partial t} + \nabla \cdot \boldsymbol{v^m} = \Psi^{mf} + \Psi^{mw}, \tag{1}$$

$$\frac{1}{M^f}\frac{\partial p^f}{\partial t} + \nabla^f \cdot \boldsymbol{v^f} = \Psi^{fm} + \Psi^{ff} + \Psi^{fw}, \tag{2}$$

where p is the pore fluid pressure (p^m in matrix and p^f in fracture), t is time, $1/M = \phi_0 C_f + (\alpha - \phi_0)/K_s$ is the inverse Biot modulus, $\alpha = 1 - (K_{dr}/K_s)$ is the Biot coefficient indicating the degree of cementation between grains, K_{dr} is the drained bulk modulus of rock, K_s is the bulk modulus of solid grains, $C_f = (1/\rho_f)d\rho_f / dp$ is the fluid compressibility from the equation of state, $\boldsymbol{v}$ is the Darcy fluid velocity vector relative to the solid skeleton, and ϵ_v is the volumetric strain. The Ψ terms indicate the mass flux transfer from fracture to matrix (superscript mf), matrix-to-fracture (superscript fm), fracture-to-fracture (superscript ff), well to matrix (superscript mw), and well-to-fracture (superscript fw). ∇^f is the nabla vector operator in the fracture domain, that is, along the 1D fracture mesh that is embedded in a 2D matrix mesh. So, the tangential divergence of an arbitrary vector quantity $\boldsymbol{\kappa}$, that is, $\nabla^f \cdot \boldsymbol{\kappa}$, in the fracture domain can be related to the divergence $\nabla \cdot \boldsymbol{\kappa}$ in the matrix domain via the projection operator as follows: $\nabla^f \cdot \boldsymbol{\kappa} = \left(\boldsymbol{I_d} - (\boldsymbol{n}^f \otimes \boldsymbol{n}^f)\right) : \nabla \cdot \boldsymbol{\kappa}$, where $\boldsymbol{n}^f$ is the fracture surface unit normal and $\boldsymbol{I_d}$ is the identity tensor. The tangential gradient operator can be defined similarly. We assume that the Biot coefficient and porosity values are the same for matrix and fracture domains. Viscosity and density of the pore fluid are also assumed to be the same in the fracture and matrix domains. The main distinction between fracture and matrix domains lies in the permeability contrast between the two media. Ignoring gravity and buoyancy effects, the Darcy velocities in the matrix and fracture domains are

$$\boldsymbol{v^m} = \frac{k^m}{\mu_f(c^m)}(-\nabla p^m), \tag{3}$$

$$\boldsymbol{v^f} = \frac{k^f}{\mu_f(c^f)}(-\nabla^f p^f), \tag{4}$$

where $\mu_f(c)$ is the concentration-dependent fluid viscosity. The fluid pressure experiences perturbations that stem from pressures at the domain boundaries, fluid flux (mass rate per unit area) across interfaces between the three domains (fracture, well, and matrix), fluid source/sink terms at the center well (mass rate per unit volume), and the volumetric strain rate which changes the fluid storage capacity of the medium. Below we discuss the closure relations for the Ψ functions.

3.2. EDFM Formulation

3.2.1. Fracture-Matrix Intersection

In EDFM formulation, pressures in the fracture and matrix domains are coupled to each other via the mass transfer functions. For closure purposes, these terms need to be expressed in terms of the pressures in the two domains. We write the matrix-to-fracture transfer function Ψ as

$$\Psi^{fm} = CI^{fm}\lambda^{fm}(p^m - p^f), \tag{5}$$

where λ^{fm} is the fluid mobility calculated as the harmonic average of the matrix cell mobility and the fracture segment mobility at their interface, CI^{fm} is the connectivity index between a matrix cell and a fracture segment, and it represents the geometrical complexity of this intersection. The fracture-to-matrix flux is assumed to be equal and opposite in sign: $\Psi^{mf} = -\Psi^{fm}$. After both the matrix and the fractures are meshed (see the numerical model section below), the discrete form of the connection mobility is

$$\lambda_{i,k}^{fm} = \frac{2\lambda_i^m \lambda_k^f}{\lambda_i^m + \lambda_k^f} \tag{6}$$

and the connectivity index is

$$CI_{i,k}^{fm} = \frac{D_{i,k}}{\langle d \rangle_{i,k}}, \tag{7}$$

where subscript i denotes a matrix cell, subscript k denotes a fracture segment, $D_{i,k}$ is the length fraction of fracture segment k inside matrix cell i, $\langle d \rangle_{i,k}$ is the calculated distance between matrix cell and fracture segment. This approach to couple fracture and matrix guarantees that the total flux between matrix and fracture is conserved.

3.2.2. Fracture-Fracture Intersection

Fracture-fracture interaction is captured via the transfer function Ψ^{ff}. The flux between two fracture segments k and l, either belonging to the same fracture or different fractures that intersect, is defined as:

$$\Psi_{kl}^{ff} = \lambda_{kl}^{ff}(p_l^f - p_k^f) \tag{8}$$

λ_{kl}^{ff} is the harmonic average of the fluid mobilities in fracture segments k and l and it is calculated similar to Equation 6. The fracture mobilities are defined similar to Moinfar et al. (2013):

$$\lambda_k^f = \frac{k^f w^f}{\mu_f \Delta x^f} = \frac{k^f \sqrt{12 k^f}}{\mu_f \Delta x^f} \tag{9}$$

Here, w^f is the fracture aperture, which is calculated from the fracture permeability k^f using the cubic law. Δx^f is the length of the fracture segment along the fracture tangent direction.

3.2.3. Fracture-Well Intersection

The flux terms Ψ^{mw} and Ψ^{fw} represent fluxes from well-to-matrix and well-to-fracture domains, respectively. Well-intersecting fractures are expected to impact the flow significantly. We define Ψ^{fw} using the Peaceman well model (Peaceman, 1978)

$$\Psi^{fw} = WI^{fw}(p^w - p^f), \tag{10}$$

where the well index WI^{fw} is calculated as in Moinfar et al. (2013)

$$WI^{fw} = \frac{2\pi k^f w^f}{\mu_f \left(\ln\left(\frac{0.14\sqrt{\left(L_f^2 + h_f^2\right)}}{r_w} \right) + s \right)} \tag{11}$$

In this equation, L_f is the fracture length in the cell, w_f is the fracture aperture, h_f is the fracture height (assumed to be equal to the thickness of the horizontal aquifer in the z-direction), r_w is the wellbore radius, and s is the wellbore skin due to near-wellbore effects such as precipitation, formation damage, non-Darcy pressure drop, etc.

3.3. Linear Momentum Balance

The linear momentum balance equations for a fluid-saturated rock under quasi-static equilibrium and in absence of body forces are

$$\nabla \cdot \boldsymbol{\sigma}^m = \mathbf{0}, \tag{12}$$

where $\boldsymbol{\sigma}^m = \boldsymbol{\sigma}'^{,m} - \alpha^m p^m \boldsymbol{I_d}$ is the Cauchy total stress tensor, and $\boldsymbol{\sigma}'^{,m}$ is the effective stress tensor. The bulk density of the matrix can be written as $\rho_b = \phi^m \rho_f + (1 - \phi^m)\rho_s$, where ρ_f is the fluid density, ρ_s is the solid grain density, and ϕ^m is the Eulerian porosity of the matrix in the current configuration. A sign convention

where the normal stresses are positive in tension and negative in compression is used. The 2D domain represents a thin layer of rock, thus a state of plane stress is assumed. In the compact engineering notation, $\boldsymbol{\sigma} = [\sigma_{xx}, \sigma_{yy}, \sigma_{xy}]^{\mathrm{T}}$, $\epsilon = [\epsilon_{xx}, \epsilon_{yy}, 2\epsilon_{xy}]^{\mathrm{T}}$, and $\boldsymbol{I_d} = [1,1,0]^{\mathrm{T}}$ are the stress, strain and identity vectors in 2D, respectively. Substituting the effective stress into Equation 12, we obtain

$$\nabla \cdot \boldsymbol{\sigma}'^{,m} - \alpha^m \nabla p^m = \mathbf{0}. \tag{13}$$

Solving the flow and the geomechanics equations simultaneously implies a full monolithic coupling between the two sub-problems. In the mechanics sub-problem, the pore pressure gradient acts as an equivalent body force that drives changes to the rock deformation and stress state. In the flow sub-problem, the matrix volumetric strain rate acts as an equivalent fluid source, or fluid storage capacity change, causing changes in the pore pressure. Assuming a linear elastic behavior of the rock, $\boldsymbol{\sigma}' = \boldsymbol{D}\epsilon$, where $\epsilon = (\nabla \boldsymbol{u} + \nabla^{\mathrm{T}} \boldsymbol{u})/2$ is the infinitesimal strain tensor defined as the symmetric gradient of the displacement vector. In the plane stress configuration, the isotropic drained elasticity tensor $\boldsymbol{D}$ can be written as

$$\boldsymbol{D} = \frac{E}{1-\nu^2}\begin{bmatrix} 1 & \nu & 0 \\ \nu & 1 & 0 \\ 0 & 0 & (1-\nu)/2 \end{bmatrix} \tag{14}$$

where E and ν are drained Young's Modulus and Poisson's Ratio of the isotropic elastic material model. The volumetric effective stress is related to the volumetric strain as $\sigma'_v = K_{dr}\epsilon_v$, where $K_{dr} = E/(2(1+\nu)(1-2\nu))$ in 2D. Mass conservation of the solid component yields the porosity evolution equation in terms of the volumetric strain ϵ_v^m and the fluid pressure p^m (Bonazzi et al., 2020; Coussy, 2004):

$$\delta\phi^m = (\alpha^m - \phi^m)\left(\delta\epsilon_v^m + (1-\alpha^m)\frac{\delta p^m}{K_{dr}}\right). \tag{15}$$

3.4. Advective Dispersive Transport

The Advection Dispersion Equations (ADE) for modeling tracer transport through matrix and fracture domains are

$$\frac{\partial(\phi^m c^m)}{\partial t} + \nabla \cdot \left(\boldsymbol{v^m} c^m - \phi^m D_d^m \nabla c^m\right) = \chi^{mf} + \chi^{mw} \tag{16}$$

$$\frac{\partial(\phi^f c^f)}{\partial t} + \nabla^f \cdot \left(\boldsymbol{v^f} c^f - \phi^f D_d^f \nabla c^f\right) = \chi^{ff} + \chi^{fm} + \chi^{fw} \tag{17}$$

where c^m and c^f are the dimensionless normalized local concentrations of the tracer in the matrix and the fracture, and D_d is the hydrodynamic dispersion coefficient assumed to be a constant. χ represents different transport fluxes across interfaces between the fracture, matrix, and well domains. During the injection episode, the well acts as a tracer source. We use an exponential model for the concentration-dependent viscosity of the mixture,

$$\mu_f(c) = \mu_1 e^{R(1-c)}, \tag{18}$$

where $c = c^m$ in the matrix and $c = c^f$ in a fracture, and $R = \log_e \frac{\mu_0}{\mu_1}$ is the log viscosity ratio of the in situ fluid viscosity μ_0 and the injected tracer viscosity μ_1. When c^m or c^f is between 0 and 1, the viscosity of the mixture is higher than the viscosity of injected tracer and lower than the in-situ fluid viscosity, for positive values of R. Here, we assume that the mixture density is independent of the tracer concentration.

3.5. Fracture Mechanics Model

The Bandis model is a widely used empirical model to provide a constitutive relationship between the state of stress and rock joint closure, which can be related to fracture hydraulic properties, that is, permeability (Barton et al., 1985). The Bandis model is based on a comprehensive laboratory investigation of the deformation behavior of a wide variety of natural unfilled joints under different loading/unloading and repeated load cycle conditions (Bandis et al., 1983). The model is especially accurate for rough joints and

fractures for which simpler models that assume smooth contacts often overestimate the shear strength (Barton & Choubey, 1977). For each fracture segment with normal direction $\boldsymbol{n}^f$, the effective normal stress $\sigma'_n = \boldsymbol{\sigma}'\boldsymbol{n}^f \cdot \boldsymbol{n}^f$, shear stress $\tau = |\boldsymbol{\sigma}'\boldsymbol{n}^f - \sigma'_n\boldsymbol{n}^f|$, and shear slip displacement δ_h are critical inputs to calculate the mechanical aperture of the segment. These equations are used to dynamically update the normal and shear stresses acting on the fracture segments using the matrix stress tensor output of the geomechanics solver and the known surface normal vectors of the segments. The slip displacement on a fracture segment is calculated using the displacement vectors of neighboring matrix nodes on either side of the fracture segment. The fracture permeability is updated based on the cubic law for flow between two parallel plates, which yields the following update relation

$$k^f = k_r^f \left(\frac{a_h}{a_{hr}} \right)^2 \tag{19}$$

where a_h is the hydraulic aperture, and subscript r indicates the reference value. The reference time is taken to be the end of the initialization period of a simulation (see initialization details below). Therefore, the reference permeability k_r^f is a function of the initial permeability k_i^f and the reference stresses at the end of initialization. Hydraulic aperture depends on the mechanical aperture and the ratio of shear displacement to peak shear displacement of each fracture segment (Barton et al., 1985; Olsson & Barton, 2001). Each fracture segment can cross multiple matrix cells, resulting in different aperture changes along its length because of the spatially changing stress tensor and slip vector corresponding to the matrix cells that the fracture segment intersects. The mechanical aperture of a fracture segment is the square root of the harmonic mean of the squared aperture of its individual parts. The mechanical aperture of a fracture segment is measured by:

$$a_m = a_0 + \Delta a_n + \Delta a_s \tag{20}$$

where a_0 is the initial mechanical aperture under zero excess effective normal stress, Δa_n is the change in mechanical aperture due to normal stress perturbation, and Δa_s is the change in mechanical aperture due to shear-induced dilation. Hysteresis in the stress-deformation behavior has not been properly accounted for in existing models. Here, we implement a hysteretic stress-deformation model that captures the difference in fracture aperture change between the loading and unloading stages of rock under compression. This model also accounts for an expected fracture permeability decrease when the well changes from injection to withdrawal, shown by lines with circle and triangle markers respectively in Figure 2. Injection corresponds to decreased compression and hence unloading of the rock, and production corresponds to loading. Based on the foundational work by Barton et al. (1985), the dependence of mechanical aperture on normal stress change is calculated as:

$$\Delta a_n = \begin{cases} \dfrac{\sigma'_n}{K_{ni}} & \text{if } \sigma'_n > 0 \left(\text{tensile state}\right) \\ \left(\dfrac{1}{V_m - V_i} - \dfrac{K_{ni}}{\sigma'_n} \right)^{-1} + V_i & \text{if } \sigma'_n \left\langle 0 \left(\text{compressive state}\right) \text{and } \delta\sigma'_n \right\rangle 0 \left(\text{unloading}\right) \\ \left(\dfrac{1}{V_m} - \dfrac{K_{ni}}{\sigma'_n} \right)^{-1} & \text{if } \sigma'_n < 0 \left(\text{compressive state}\right) \text{and } \delta\sigma'_n < 0 \left(\text{loading}\right) \end{cases} \tag{21}$$

where V_i is the irrecoverable closure that contributes to the hysteretic behavior and $\delta\sigma'_n$ is the incremental normal effective stress between consecutive time steps. K_{ni}, V_m, and V_i are defined in the caption of Figure 2 and readily calculated using empirical correlations in Barton (1982). Our implementation has notable improvements compared to the original model in evaluating peak shear displacement (δ_{peak}), post-peak shear strength (B-C in the top right quadrant of Figure 2), aperture closure at small shear displacement, and fracture surface degradation. The model parameters are functions of the input parameters of the original Bandis model, which are the joint roughness coefficient (JRC), joint compressive strength (JCS), and Unconfined Compressive Strength UCS. JRC determines the shear strength of unfilled hard rock joints. It can be estimated by comparing the appearance of a discontinuity surface with standard profiles published in Barton (1982). JCS signifies the degree of weathering of the rock joint and can be estimated by the use of the Schmidt rebound hammer test. If the joints are completely unweathered, then JCS will be equal to the UCS of the unweathered rock. As the joints get weathered and weakened, JCS decreases accordingly. In addition to modeling the aperture closure dependency on the fracture normal stress, we also incorporate a

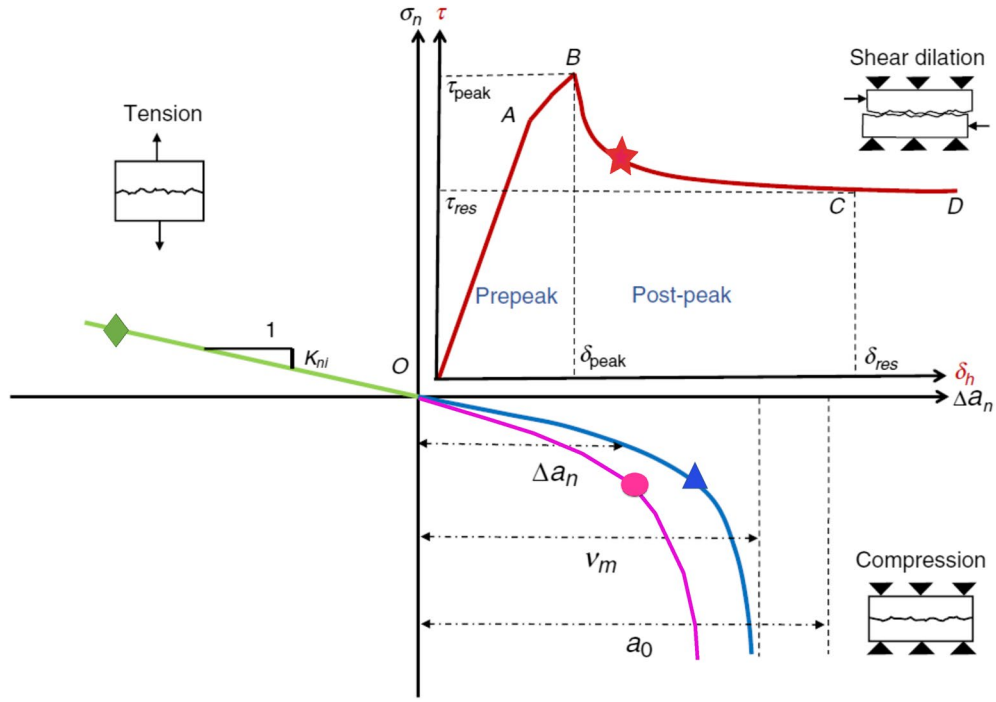

Figure 2. The modified Bandis model to model nonlinear fracture mechanics in response to dynamically evolving normal and shear stresses (S. Li et al., 2017). The top left quadrant shows the behavior of a fracture in tension with K_{ni} denoting the initial normal fracture stiffness. The bottom right quadrant shows a fracture in compression, displaying the initial mechanical aperture a_0 under zero excess effective normal stress, the maximum aperture of the fracture under compression (V_m), and the change in mechanical aperture Δa_n due to normal stress perturbation. Hysteresis within a loading-unloading cycle on the fracture is shown with the triangle marker (loading or withdrawal period) and the circle marker (unloading or injection period) lines. The upper right quadrant shows the dependence of shear stress (τ) on shear displacement (δ_h). The mobilization of JRC is divided into the pre-peak and post-peak periods, separated by point B corresponding to peak shear displacement δ_{peak} and peak shear strength τ_{peak}. As the shear displacement increases to the residual shear displacement δ_{res}, the residual shear strength τ_{res} is slowly reached at points C and D (upper right quadrant).

shear-related physical mechanism that alters hydraulic aperture. We take into consideration the reduction of post-peak shear strength from fracture surface degradation and shear-induced dilation. The shear-induced dilation is formulated as a function of δ_h (Asadollahi & Tonon, 2010):

$$\Delta a_s = \begin{cases} \left(\dfrac{2\delta_h^2}{3\delta_{peak}} - \dfrac{\delta_h}{3}\right)\tan\left[\mathrm{JRC}\cdot\log\left(\dfrac{\mathrm{JCS}}{\sigma_n'}\right)\right] & \text{if } \delta_h < \delta_{peak} \\ \Delta a_{v,peak} + \delta_{peak}\int_1^{\delta_h/\delta_{peak}} \tan\left[\mathrm{JRC}_p\cdot\log\left(\dfrac{\mathrm{JCS}}{\sigma_n'}\right)\cdot x^{-0.381}\right]dx & \text{if } \delta_h > \delta_{peak} \end{cases} \quad (22)$$

where x and dx are dummy variables of integration, δ_{peak} is the peak shear displacement, $\Delta a_{v,peak}$ is the peak shear-induced dilation, JRC_p is the peak joint roughness coefficient, and log refers to base-10 logarithm. These parameters are readily calculated based on the correlations given in Asadollahi and Tonon (2010). The shear-induced effect is integrated during the injection episodes only, with the parameters tuned to yield a reasonable relative change in permeability based on the experimental work of Ye and Ghassemi (2018). Fractures tend to slip during the injection period when the effective normal compression on a fracture decreases. One of the limitations of our model is a lack of feedback from fracture slip to stress relaxation, that is, the coupling between fracture dynamics and mechanical equilibrium (Equation 13) is one-way only (Figure 3). This can be justified based on the computational expense of solving the nonlinear contact problem on each of the fractures, many of which intersect each other, coupled to the equilibrium equations. One-way coupling has been used successfully in other transport studies (e.g., Sweeney & Hyman, 2020). The cou-

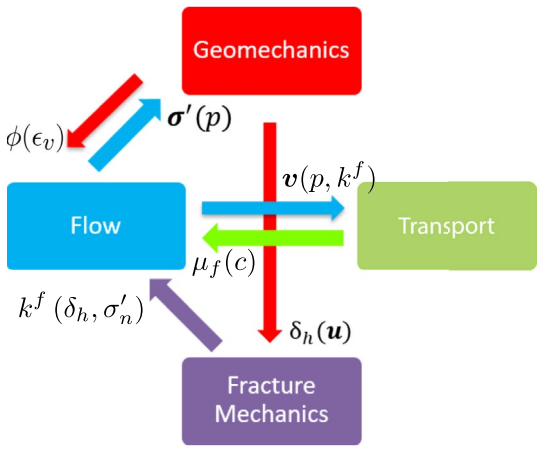

Figure 3. Flow and geomechanics are coupled two-way through the strain-dependent porosity $\phi(\epsilon_v)$ in the fluid mass balance equation (Equation 1) and the fluid pressure-dependent effective stress $\boldsymbol{\sigma}'(p)$ in the linear momentum balance equation (Equation 13). The flow and transport are coupled two-way through the concentration-dependent fluid viscosity $\mu_f(c)$ and pressure-dependent velocity field $\boldsymbol{v}(p)$. Geomechanics is coupled one-way with fracture mechanics by providing the nodal displacement, stress, and strain tensors to the Bandis model for slip activation, slip magnitude calculation, and fracture aperture update. Fracture mechanics delivers updated stress-dependent permeability $k^f(\delta_h, \boldsymbol{\sigma}'_n)$ to the flow solver based on shear slip δ_h and normal dilation, which is dependent on the effective normal stress $\boldsymbol{\sigma}'_n$.

pling from fracture slip to domain-wide stresses can be important for long fractures slipping across their entire length and for propagating fractures, where an accurate calculation of induced seismic event time and magnitude may require an estimation of stress relaxation (Jha & Juanes, 2014; Meguerdijian & Jha, 2021; X. Zhao & Jha, 2021). To resolve this partially, we imposed a limit on the maximum number of times a fracture segment is capable of slipping, and we set this limit to be equal to the number of sub-segments this fracture is divided into when intersecting the matrix mesh cells. Figure 2 illustrates our fracture mechanics model.

3.6. Initial and Boundary Conditions

The coupled flow, transport, and geomechanics problem requires suitable boundary conditions for the three sub-problems. Referring to the physical model in Figure 1, we apply the following boundary conditions: zero normal displacement on the bottom and right boundaries, compressions on the left and top boundaries with a prescribed stress anisotropy due to regional tectonics, zero normal fluid flux on the left and right boundaries, fixed pressures on the top and bottom boundaries which may represent constant pressure of producing wells at those locations, and the natural outflux boundary condition for the tracer transport problem. The cyclic well in the domain is controlled by a prescribed injection rate q_{inj} until the tracer breaks through at the boundary. This is followed by a soaking period of 30 days when only the in situ fluid is injected. Finally, the tracer withdrawal episode is modeled by a prescribed well withdrawal rate q_{prod} for 90 days. Units of q_{inj} and q_{prod} are volumetric rates per unit length in the third dimension.

Initialization of a coupled flow-transport-geomechanics problem, especially in low permeability rocks with highly conductive fractures, is a challenging task. This is also true during lab experiments involving such rocks, for example, initialization of pressure and concentration fields in a shale core subjected to coreflooding can take days. The goal of initialization is to achieve mechanical and hydrostatic equilibria such that the initial strains and fluid fluxes inside the domain are zero in absence of sources/sinks (i.e., wells). Spatially uniform fields of pressure, concentration, stresses, and displacements, for example, zero excess pressure and displacements combined with initial stresses equal to boundary tractions, are prescribed as initial conditions that are close to, but not exactly at, the equilibrium. During the initialization period of the simulation, we solve the governing equations with the prescribed boundary compressions, initial conditions, body forces (in case of a 3D model), and initial rock-fluid properties to achieve the state of poromechanical equilibrium. No wells or tracers are active during the initialization period. The state variables, for example, pressure and stress, at the end of initialization become our reference state. Stress-dependent properties such as porosity and permeability fields also experience perturbations during initialization and change from their initial user-prescribed values. We define "excess" quantities, for example, excess pressure, at a time as the difference between the value at and the value at the reference time. The cyclic well starts operating at the end of the initialization period with a fixed tracer concentration prescribed at the well location.

This completes the definition of the coupled problem. The governing equations to be solved are Equations 1, 2, and 13 (after substitution to express it in terms of displacements), Equations 16 and 17 subject to the initial and boundary conditions mentioned above. The constitutive equations for the fluid compressibility, tracer viscosity, stress-strain relation, well connectivity, mass transfer fluxes, and fracture mechanics provide the necessary closure of the system of equations. It is a nonlinear system of coupled differential equations with multiple length and time scales that correspond to multiple physical mechanisms in the system. As mentioned earlier, we select pore fluid pressures p^m and p^f, displacement vector $\boldsymbol{u}$, and concentrations c^m and c^f as the primary unknowns of the problem. The effective stress $\boldsymbol{\sigma}'$, porosity ϕ, Darcy velocities $\boldsymbol{v^m}$ and $\boldsymbol{v^f}$, fracture aperture a_h, and permeability k^f are the secondary variables which we update explicitly by post-processing the primary variables.

4. Numerical Model

Solving the coupled problem defined above requires a numerical discretization scheme that can honor the continuity requirements of the primary and secondary variables while allowing for multiple scales in the discrete system. Computational efficiency and robustness are the other two requirements on the numerical model because we intend to apply the model to aquifers with geometrically complex fracture networks, such as the one shown in Figure 1 with more than 20 fractures of arbitrary lengths and orientations intersecting each other. To satisfy these requirements, we use the finite volume method to discretize the flow and transport equations, and the Galerkin finite element method to discretize the mechanics equations (Jha & Juanes, 2014; Tran & Jha, 2020). We discretize the domain using an n_d-dimensional uniform Cartesian mesh ($n_d = 2$ for 2D case). The fractures are discretized uniformly on a separate $n_d - 1$ dimensional mesh. The weak forms of the flow and mechanics equations are obtained by following the standard variational recipe: multiply the strong form by an appropriately defined smooth test function, integrate the equation over the domain, apply integration by parts and reduce the order of differentiation on the primary unknown, apply the divergence theorem, and impose Neumann boundary conditions (Tran & Jha, 2020). We use cell-centered piecewise constant pressure and concentration degrees of freedom and bilinear functions with nodal displacement degrees of freedoms. This choice satisfies the inf-sup condition because we consider a compressible system with finite values of the solid grain compressibility $1/K_s$ and the fluid compressibility C_f, which are typical of most subsurface formations and deep aquifers. The Darcy flux term in the flow equation is linearized using the two-point flux approximation. The advective flux term in the ADE is discretized using upwinding and the central finite difference is used to discretize the diffusive flux term. We use the first-order accurate Backward Euler method to implicitly integrate the flow equations in time. Finally, we obtain the linear system of equations to be solved at each time step.

4.1. Coupling Strategy and Solution Scheme

Our coupled computational framework consists of four parts: geomechanics, flow, transport, and fracture mechanics (Figure 3). Each component is connected to at least one other component via a one-way or two-way coupling link. The strength of coupling is dictated by different parameters: α, E, C_f for flow-geomechanics coupling; R, k^f for flow-transport coupling; and JRC, JCS for fracture mechanics-geomechanics coupling.

We utilize a fully coupled simultaneous solution approach to solve for displacement and pressure fields at each time step (Jha & Juanes, 2007; Lewis & Sukirman, 1993; Tran & Jha, 2020). The matrix-vector system of linear equations becomes

$$\begin{bmatrix} \boldsymbol{K} & -\boldsymbol{Q} & 0 & 0 \\ \boldsymbol{Q}^T & \boldsymbol{S}^m + \delta t \boldsymbol{A}^m & -\delta t \boldsymbol{T}^{mf} & -\delta t \boldsymbol{T}^{mw} \\ 0 & \delta t \boldsymbol{T}^{fm} & \boldsymbol{S}^f - \delta t \boldsymbol{A}^f & \delta t \boldsymbol{T}^{fw} \\ 0 & \boldsymbol{T}^{wm} & \boldsymbol{T}^{wf} & -\boldsymbol{A}^w \end{bmatrix} \begin{bmatrix} \boldsymbol{U}^m \\ \boldsymbol{p}^m \\ \boldsymbol{p}^f \\ \boldsymbol{p}^w \end{bmatrix}^{n+1} = \begin{bmatrix} \boldsymbol{f}^{\boldsymbol{u}} \\ \delta t \boldsymbol{f}^{\boldsymbol{p},\boldsymbol{m}} + \boldsymbol{Q}^{\boldsymbol{T}} \boldsymbol{U}^{m,n} + \boldsymbol{S}^m \boldsymbol{p}^{m,n} \\ \delta t \boldsymbol{f}^{\boldsymbol{p},\boldsymbol{f}} - \boldsymbol{S}^f \boldsymbol{p}^{f,n} \\ \boldsymbol{q}^{\boldsymbol{w}} \end{bmatrix} \tag{23}$$

where $\boldsymbol{U}$ is the vector of nodal displacements from the finite element interpolation $\boldsymbol{u} = \boldsymbol{N}^T \boldsymbol{U}$, $\boldsymbol{N}$ is the matrix of bilinear shape functions; $\boldsymbol{p}^{\boldsymbol{m}}$, $\boldsymbol{p}^{\boldsymbol{f}}$, and $\boldsymbol{p}^{\boldsymbol{w}}$ are the vectors of cell-centered matrix pressure, fracture segment pressure, and well segment pressure unknowns respectively, n is the previous time step, and $n+1$ is the current time step at which displacements and pressures are solved such that $\delta t = t^{n+1} - t^n$. The global stiffness matrix is assembled from element stiffness matrices,

$$\boldsymbol{K}_i = \int_{\Omega_i} \boldsymbol{B}_i^{\mathrm{T}} \boldsymbol{D}_i \boldsymbol{B}_i \, d\Omega \tag{24}$$

where $\boldsymbol{B}$ is the strain-displacement matrix computed by applying the symmetric gradient operator to $\boldsymbol{N}$, and i is the element or cell index. There are two kinds of transmissibility matrices in Equation 23. The global transmissibility matrix $\boldsymbol{A}$ is assembled from interfaces between cells of a single medium, indicated by the superscript m, f, or w in the equation. The global transmissibility matrix $\boldsymbol{T}$ is assembled from the individual interface transmissibilities between two different media, which are indicated by the two superscripts mf, wf, and mw in the equation. See our earlier paper (Tran & Jha, 2020) for expressions of the transmissibility

matrices. The global storativity or compressibility matrix $\boldsymbol{S}$ for either the matrix or the fracture is a diagonal matrix with components, $S_{ii} = \int_{\Omega_i} 1/M_i \, d\Omega$. The flow-geomechanics coupling matrix at the element level is,

$$\boldsymbol{Q}_i = \int_{\Omega_i} \alpha \boldsymbol{B}_i^{\mathrm{T}} \boldsymbol{I}_{\boldsymbol{d}} \, d\Omega. \tag{25}$$

The right-hand side of the weak form of the mechanics problem $\boldsymbol{f}^{\boldsymbol{u}}$ consists of traction (and body forces in case of a 3D model),

$$\boldsymbol{f}^{\boldsymbol{u}} = \int_{\Gamma_t} \boldsymbol{N}^{\mathrm{T}} \overline{\boldsymbol{\sigma}} \, d\Gamma + \int_{\Omega} \boldsymbol{N}^{\mathrm{T}} \rho \boldsymbol{g} \, d\Omega \tag{26}$$

where Γ_t denotes Neumann boundaries of the domain with the prescribed tractions $\overline{\boldsymbol{\sigma}} = [0, \sigma_H]^{\mathrm{T}}$ on the top boundary and $\overline{\boldsymbol{\sigma}} = [\sigma_h, 0]^{\mathrm{T}}$ on the left boundary. The right-hand side of the weak form of the flow problem $\boldsymbol{f}^{\boldsymbol{p}}$ consists of prescribed fluxes and well terms. We solve Equation 23 using a direct solver. The Darcy velocity field is computed from the pressure solution. Next, the ADE is solved for the unknown concentrations. The flow-geomechanics problem is solved again at the same time step with the new concentration and fluid mobility fields. This process is repeated iteratively within an inner loop inside the time loop until pressure, concentration, and displacement solutions converge at the specified time step. The coupling between the poroelastic solver and the transport solver is implemented using a sequential one-way coupled approach. For the range of R considered in this study, the transport-to-deformation coupling strength is expected to be weak because there is no direct effect of concentration on the mechanics Equation 13, and the effect of concentration on pressure is limited to fluid mobility. For the range of parameter values considered, the inner loop takes less than seven iterations to achieve convergence at any time step during the course of the simulation.

5. Model Verification and Benchmarking

In recent literature, EDFM has been successfully validated against traditional methods of fracture modeling, for example, EDFM's pressure solutions are compared to pressure solutions from discrete fracture network simulations of multiphase flow in complex fracture networks (Hajibeygi et al., 2011; Shakiba, 2014). Further validation studies have been conducted using both a fine-grid simulation and a semi-analytical solution (Jansen et al., 2018; Shakiba, 2014). We conducted two model verification studies, shown in Figures S1 and S2 in Supporting Information S1, where we compare our EDFM pressure solution with a commercial multiphysics simulator solution and an analytical solution, respectively. Below we present results from benchmarking on the Mandel consolidation problem to verify poroelastic coupling in our framework.

5.1. Mandel-Cryer Effect

To test the accuracy of poroelastic coupling in our computational framework, we applied the framework to the classic Mandel problem. An elastic, isotropic, homogeneous rock slab that is infinitely long in the z-direction is constrained between two frictionless, impermeable rigid plates (Figure 4). Due to the symmetry of the problem, the computational domain can be limited to the upper right quadrant (shaded gray in the panel [a] of Figure 4) with size $L_x \times L_y$. The sudden application of compression at the boundary results in a positive excess pressure and linear displacements in the domain, also known as the undrained deformation, because the pore fluid does not have sufficient time to drain yet. The vertical left and right boundaries at $x = \pm L_x$ (or dimensionless x-coordinate $x_d = \pm 1$) are free to deform at ambient pressure, which allows the fluid to drain over time. This implies that $x = 0$ can be modeled as a roller boundary condition. The analytical expressions of pressure, displacement, and stress are given in the literature (Abousleiman et al., 1996; Castelletto et al., 2015). Figure 4b shows the dimensionless pressure profile along the horizontal distance in the shaded domain at four dimensionless time steps. The dimensionless pressure p_d is obtained by normalizing the pressure by $p_0 = FB(1 + \nu_u)/(3L_x)$ where $B = \nu/(\nu^2 + (K_{dr}/M))$ is the Skempton coefficient and $\nu_u = (3\nu + B\nu(1 - 2\nu))/(3 - B\nu(1 - 2\nu))$ is the undrained Poisson's ratio. At early times ($t_d < 0.1$), the $x = L_x$ boundary becomes softer due to pressure dropping from fluid drainage at that boundary. The stress is transferred inwards into the domain, which is a stiffer region than the drainage boundary. This causes the pressure near the $x = 0$ boundary to increase above the undrained pressure value, that is, $p_d > 1$, which is known as the Mandel-Cryer effect. Next, we discuss results from a few representative numerical simulations.

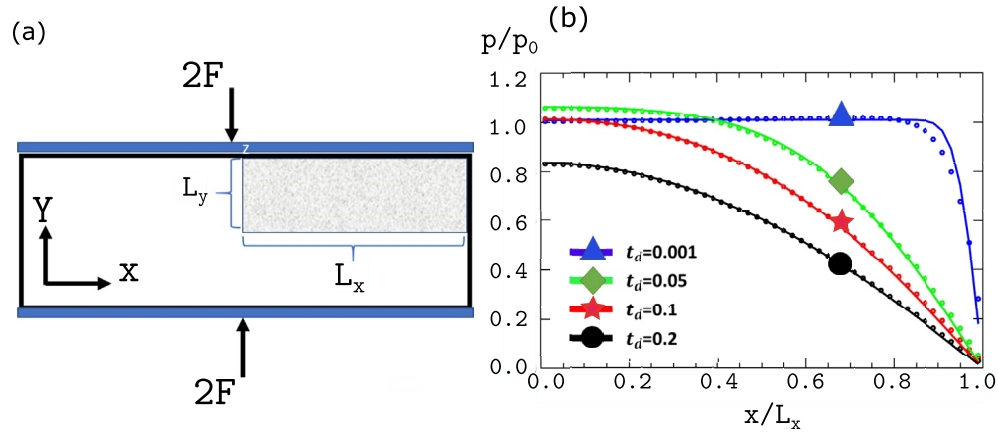

Figure 4. (a) The Mandel problem setup with the origin of the *x*-*y* coordinate system positioned at the center of a plane strain 2D slab of dimension $2L_x \times 2L_y$. Symmetry allows modeling of a quarter of the slab, producing a computational domain of size $L_x \times L_y$. The system is under a compressive vertical force denoted as $2F$ applied instantaneously at $t = 0$. (b) The dimensionless pressure p/p_0 versus the dimensionless *x*-coordinate $x_d = x/L_x$ at different dimensionless times t_d. The lines show the simulation results and the dots are the analytical solutions. The simulation agrees with the analytical result and captures the Mandel-Cryer effect at the early time step of $t_d = 0.05$.

6. Results

All simulation cases below follow the same operational sequence for the cyclic well: the well starts injecting tracer until the tracer breaks through at either the top or bottom boundary, then the well injects the in-situ fluid for the 30-day soaking period, and finally, the well withdraws fluids for the 120-day withdrawal period. The withdrawal rate is set at 1.5 times the injection rate, which is typical in a push-and-pull test.

6.1. Base Case

We define a base case using the values of the mesh, initial condition, and boundary condition parameters shown in Table 2, together with the material parameter values shown in Table 3. Some of these values are taken from a published tracer flowback case study (J. Li et al., 2016). Utilizing the proposed computational framework, we analyze the base case results to identify the key characteristics of flow, transport, and geomechanical behavior.

6.1.1. Transport Response in a Coupled Flow-Geomechanics Framework

The tracer distribution in the matrix (colored contour lines) and fracture (colored straight lines) are monitored at three selected time steps: end of injection which is also the tracer breakthrough time, end of soaking, and end of 30-day withdrawal (Figure 5). During injection, the effect of the fracture network becomes evident as the tracer advects along the fractures that intersect the wellbore. Some amount of tracer directly enters the matrix due to diffusion. Tracer diffusion is also observed across the fracture-matrix interfaces, especially the ones situated within the viscous fingers of tracer that protrude outward from near-well fractures. Among the fractures that intersect the well, there exists a preferential direction for the movement of the tracer based on the orientation of the fractures. Due to the coupling between the tracer viscosity and the pressure field, this preferential transport controls how much the fracture permeability changes with the in situ stress field. The more favorably aligned a fracture is to the regional principal stress directions (in this case, fractures oriented quasi-parallel to S_H, that is, orthogonal to S_h), the more penetrating the fracture's tracer distribution is. In fact, the tracer breaks through at the bottom boundary by flowing through the most vertically oriented fracture in the bottom right of the domain (panel [a] of Figure 5). During the soaking period, since there is no additional tracer injected, the tracer concentration field displays a more spread-out distribution in the aquifer with smaller tracer concentration values around the well. The main transport mechanism is diffusion across matrix-fracture and matrix-matrix interfaces, which contributes to less pronounced tracer fingers. The pressure field is continuous but not necessarily smooth across a fracture, demonstrated by the kinks in the pressure contours as seen by the bottom panels in Figure 5. During the

Table 2
Simulation Parameters

Parameter	Symbol	Value
Number of cells in the x-direction	N_x	100
Number of cells in the y-direction	N_y	100
Number of cells in the z-direction	N_z	1
Domain length in the x-direction	L_x	200 m
Domain length in the y-direction	L_y	200 m
Domain length in the z-direction	L_z	75 m
Top boundary compression	S_H	82 MPa
Left boundary compression	S_h	50 MPa
Initial excess pressure	Δp_0	0 MPa
Initial pressure	p_0	35 MPa
Prescribed top and bottom boundary pressure	p_{out}	35 MPa
Well injection rate	q_{inj}	7.4×10^{-5} m^3/sec/m
Well production rate	q_{prod}	11.1×10^{-5} m^3/sec/m
Poisson's ratio	ν	0.27
Solid grain density	ρ_s	2,650 kg/m^3
Drained bulk modulus (matrix and fracture)	K_{dr}	21.9 GPa
In situ fluid viscosity	μ_0	1.2×10^{-3} Pa-sec
Injected tracer viscosity	μ_1	0.16×10^{-3} Pa-sec
Fluid density	ρ_f	1,000 kg/m^3
Matrix permeability	k^m	5 millidarcy
Initial fracture permeability	k_0^f	1,256 darcy
Initial matrix porosity	ϕ_0^m	0.1
Fracture porosity	ϕ^f	0.1
Unconfined compressive strength	UCS	150 MPa

tracer withdrawal period, the fracture network again shows its impact on the tracer distribution as displayed by the increased spacing between the tracer contours, despite a lower value of the concentration gradient inside the fracture compared to the injection period.

Table 3
Base Case Parameters

Parameter	Symbol	Value
Drained Young's modulus	E	25.55 GPa
Biot modulus	M	16.9 GPa
Diffusion coefficient	D_d	2×10^{-7} m^2/sec
Fluid compressibility	C_f	0.5×10^{-9} Pa^{-1}
Biot coefficient	α	0.5
Log viscosity ratio	R	2
Joint compressive strength	JCS	130 MPa
Joint roughness coefficient	JRC	8

The tracer retrieval data is available in most tracer survey studies, which can yield useful information, if used correctly. The tracer retrieval curve can be used to deduce fracture morphology (J. Li et al., 2016), especially if the fracture network is complex with spatially non-uniform fracture density (number of fractures per unit length or volume), orientation, and permeability. The temporal characteristics of tracer retrieval curves at various locations along the horizontal well are shown in Figure 6. During the early period of injection ($t < 5$ day), concentration around the well rises sharply to reach a peak level of $c^w \approx 0.5$, and the fractures intersecting the well are saturated with the tracer. Then the tracer level increases at a much slower rate and the tracer slowly diffuses into the matrix through matrix-matrix or fracture-matrix interfaces. As expected, during the soaking period when the well does not inject any tracer, the tracer concentration level at the well drops sharply to zero. The soaking period shows minimal differences in c^w values between different well locations due to a lack of tracer injection into the domain during this period. During withdrawal, a more gradual build-up

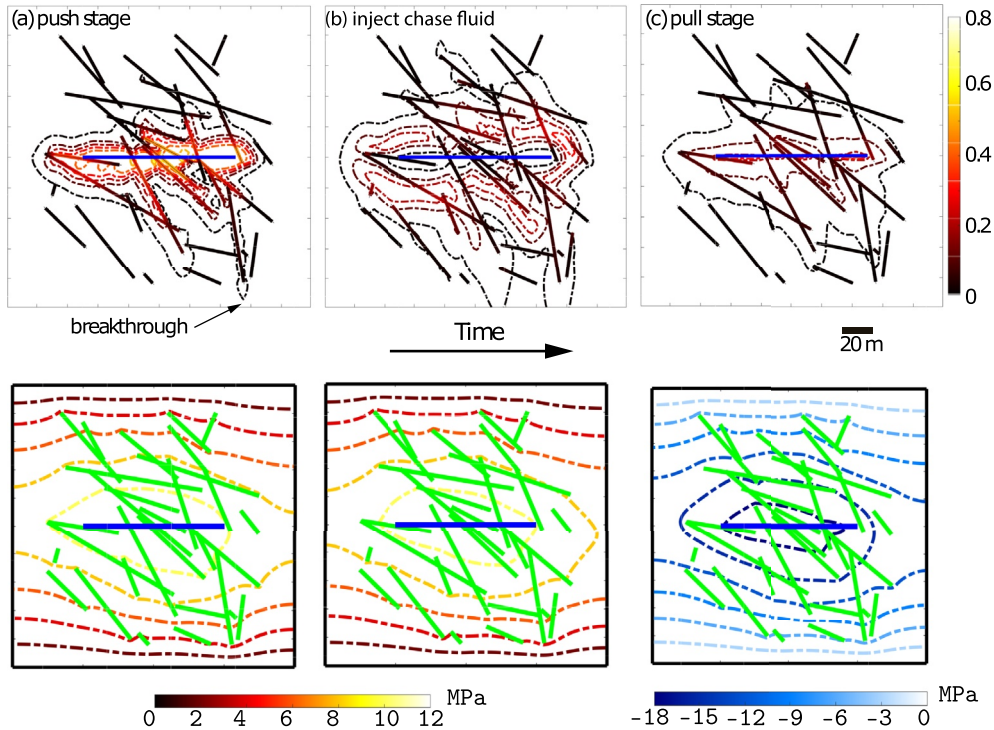

Figure 5. Top row: Tracer concentrations in fractures and in the matrix at three successive time steps of the base case model: (a) at tracer breakthrough (t_{BT}) which is also the end of injection period, (b) at the end of the chase fluid injection period (soaking), and (c) 30 days into the withdrawal period. The well is denoted by the blue horizontal line. Matrix concentration c^m is shown via contours drawn at an increment of 0.1. Fracture concentration c^f is shown via colored straight lines drawn along the fracture length. Both follow the same color scale shown on right. The shape and size of the contours are controlled by the connectivity of the well to the fractures and by the transport processes. Bottom row: corresponding excess pore pressure distribution at the three selected time steps. Different color scales have been used for the push and pull periods to account for the sign reversal of the excess pore pressure during push and pull periods.

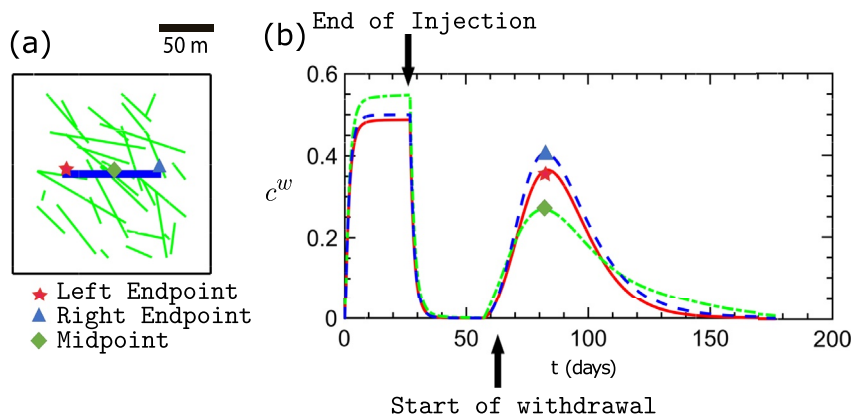

Figure 6. Evolution of the tracer concentration at three selected points along the well. The curves at the right and left ends of the well are similar during the injection period while the middle point shows a higher concentration due to a higher fracture density near the center. The soaking period does not show any distinction among the three curves because the tracer is neither injected nor withdrawn. The withdrawal period curves are more separated from each other compared to the injection period because both advection and diffusion processes feel the fracture morphology deeper in the aquifer during later periods.

is observed as the tracer returns to the well. Transport is non-uniform along the length of the well due to a non-uniform fracture density along the length of the well. This is true in our study as indicated by Figure 1: the left and right thirds of the wellbore have fewer fractures compared to the middle third of the well. Since fractures contribute significantly to the advective transport, which is away from the well during injection and toward the well during withdrawal, the middle point curve shows a higher peak concentration during injection and a lower peak concentration during withdrawal compared to the curves at the endpoints (Figure 6).

An interesting observation is an increase in separation between the three curves during the withdrawal period compared to injection. This points to hysteresis in advective transport through a medium with discrete fractures. Here, hysteresis refers to the observation of different concentrations at a point as the direction of flow reverses, for example, due to switching the well from injection to withdrawal. Hysteresis in diffusion-dominated transport is well-understood because the effect of diffusion on the concentration gradient at a point is monotonic with time, even if the flow direction reverses. However, hysteresis in advection-dominated laminar flow (high Peclet number and low Reynolds number) is a topic of research and has many applications in the mixing industry, for example, in microfluidics. Our study setup allows us to observe, quantify and control the magnitude of hysteresis in tracer transport through a fractured aquifer. Separation of the three concentration profile curves, which correspond to regions with three different fracture densities, also suggests that these observables have a diagnostic use. If such c versus data is acquired in the field by zonal fluid sampling along the wellbore at multiple time steps, the curves can be used to quantify the fracture density in the aquifer away from the well. This is valuable because electrical resistivity-based fracture logging tools sense only 1–6 inches away from the wellbore. The fracture density in the left and right segments of the well are similar, yet there exists a slight difference between the two tracer retrieval curves. This is due to the difference in the fracture orientations of these two segments: the orientations are more orthogonal to S_H in the left segment than in the right segment (Figure 6). The variation in fracture orientation determines the action of the stress tensor on these discontinuities, resulting in different permeability changes and a variation in the tracer retrieval curves. The impact of fracture permeability and orientation on the tracer retrieval curve will be revisited in later sections because they are strongly related to the stress field.

6.1.2. Stress Response to Pressure Coupling

Next, we analyze how induced stresses in the aquifer vary with time and space during the episodic transport. The isotropic part of the deformation (volumetric expansion or contraction) is quantified by ϵ_v^m which is controlled by the effective volumetric stress $\sigma_v^{',m}$, which is related to the total volumetric stress $\sigma_v^m = \text{trace}(\boldsymbol{\sigma}^m)/n_d$ as $\sigma_v^{',m} = \sigma_v^m + \alpha^m p^m$. The deviatoric part of deformation is controlled by the von Mises stress $\sigma_{VM}^m = \sqrt{3J_2}$, where J_2 is the second invariant of the deviatoric stress tensor $(\boldsymbol{\sigma}^m - \sigma_v^m \boldsymbol{I_d})$ with $\boldsymbol{I_d}$ is the identity tensor (Tran & Jha, 2020). To characterize the state of stress in the domain, three different stress quantities are chosen: effective volumetric stress $\sigma_v^{',m}$ for isotropic deformation, von Mises stress σ_{VM}^m, and poroelastic shear stress invariant $I_{MC}^{'}$ for shear-induced rock failure and plasticity. With the effective stress $\boldsymbol{\sigma}^{',m}$ denoted in Voigt engineering notation as $[\sigma_{xx}^{'},\sigma_{yy}^{'},\sigma_{xy}^{'}]^{\mathrm{T}}$, the von Mises stress for the plane stress condition is defined as follows:

$$\sigma_{VM}^{'} = \left[(\sigma_{xx}^{'})^2 + (\sigma_{yy}^{'})^2 - \sigma_{xx}^{'}\sigma_{yy}^{'} + 3(\sigma_{xy}^{'})^2\right]^{1/2} \tag{27}$$

The excess poroelastic shear stress $I_{MC}^{'}$ is calculated as a function of the first and second stress invariants $I_1^{'}$ and $\sqrt{J_2^{'}}$, representing the invariant form of the Mohr-Coulomb (MC) yield function (Borja, 2013).

$$I_1^{'} = 2\sigma_v^{',m} \tag{28}$$

$$J_2^{'} = \frac{1}{6}[(\sigma_{xx}^{'} - \sigma_{yy}^{'})^2 + \sigma_{xx}^{',2} + \sigma_{yy}^{',2}] + \sigma_{xy}^{',2} \tag{29}$$

$$I_{MC}^{'} = \sqrt{J_2^{'}} - \frac{1}{3} I_1^{'} \sin\left(\arctan(\mu_s)\right), \tag{30}$$

where μ_s is the static frictional coefficient of the host rock. The temporal evolution of excess pressure and stress quantities are shown in Figure 7 at three locations: near the midpoint of the well (left diagram), the center of the upper half of the domain (middle diagram), and near the top boundary (right diagram). At the very beginning

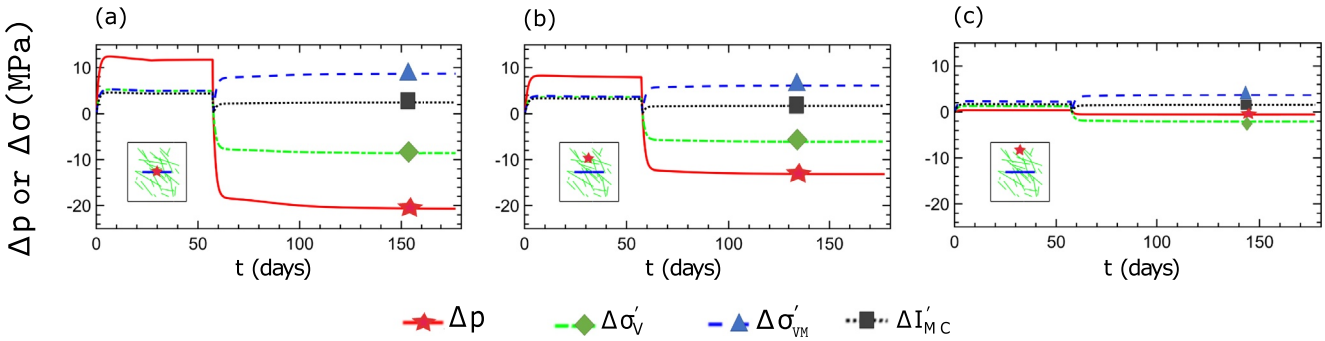

Figure 7. The temporal evolution of excess pore pressure (Δp) in the matrix, excess effective volumetric stress ($\Delta\sigma_v'$), and excess Mohr-Coulomb stress Invariant ($\Delta I_{MC}'$) at different locations in the domain, which are marked in the inset figures in the bottom left. The locations are (a) near the midpoint of the well, (b) center of the upper half of the domain, and (c) near the top boundary. Pressure (star marker), Mohr-Coulomb stress invariant (black marker), Von Mises stress (blue marker), and effective volumetric stress (diamond marker) evolve with time as the well goes through tracer injection, soaking (or chase fluid injection), and withdrawal episodes.

of the injection period, pressure rises due to the introduction of tracer fluid in a low permeability reservoir. The pressure then stabilizes and starts decreasing slightly because the injected tracer has a lower viscosity than the in situ fluid it displaces in the domain. The pressure plateaus during much of the soaking period as no additional tracer is introduced. Then during the withdrawal period, the excess pressure turns negative, meaning the pressure is lower than the initial pressure. This is expected as the fluids drain from the domain into the well. The negative excess pore pressure continues to decrease throughout the withdrawal period as more tracer is displaced from the domain and replaced by the viscous resident fluid encroaching from the boundaries.

Quantities characterizing the stress state evolve synergistically with the excess pore pressure in the matrix (Figure 7). Temporal evolution of the volumetric, deviatoric (von Mises), and Mohr-Coulomb first invariant stresses follow the excess pressure trend closely, confirming that the pressure field is driving the coupled dynamics of the system. During the injection period, pore pressure is higher than the initial pressure (positive excess pore pressure or $\Delta p > 0$), leading to a decrease of the effective volumetric stress, which means the host rock becomes more tensile. Because of the sign convention of the compressive state of the reservoir ($\sigma_v'^{,m} < 0$), this means that the excess effective volumetric stress is positive ($\Delta\sigma_v'^{,m} > 0$) as shown by the lines with the diamond marker in Figure 7. A similar argument can be made during the withdrawal period. As the rock becomes more volumetrically compact during production, the $\Delta\sigma_v'^{,m}$ behavior mirrors the trend of Δp. Investigating the rich and complex spatial and temporal evolution of σ_v' is important in practical applications. For example, in designing a new infill hydraulically fractured well, an optimal strategy is to choose drilling targets in a low compressive stress environment to facilitate the opening of stimulated fractures (Guo et al., 2019). Besides the reversal of excess volumetric stress and excess pore pressure between injection and withdrawal periods, excess Von Mises stress and excess poroelastic shear stress are positive throughout these two episodes due to their definitions in Equation 30. Near the injection well, the Von Mises stress is very close to the excess effective volumetric stress because the excess shear stress is small compared to the excess effective normal stress ($\Delta\sigma_{xy}' \ll \Delta\sigma_{xx}'$) and the stress state is almost isotropic ($\Delta\sigma_{xx}' \approx \Delta\sigma_{yy}'$) (panels [a and b] of Figure 7). Under these conditions, Equation 27 becomes $\sigma_{VM}' \approx [(\sigma_{xx}')^2 + 3(\sigma_{xy}')^2]^{1/2} \approx \sigma_{xx}'$. However, as we move away from the center of the domain to regions where the excess pressure perturbation is minimal and the magnitude of $\Delta\sigma_{xy}'$ grows in comparison to $\Delta\sigma_{xx}'$, $\Delta\sigma_{VM}'$ dominates $\Delta\sigma_v'$. This suggests that shear-induced deformation becomes dominant away from the well as shown in the separation of the curves with triangle and diamond markers. This can be explained by less tension (quantified by I_1'), or the increasing prominence of remote shear components (quantified by $\sqrt{J_2'}$), or both, as we move away from the injection well. The injection-induced rock expansion around the injection well is accompanied by slight compression at the boundary.

The directional re-alignment of maximum and minimum horizontal principal stresses due to pressure perturbation is of importance for the optimal design of a hydraulic fracturing job and well trajectory layout. When an existing well is operated cyclically as an injector and producer, the operator has to estimate the change in the principal stress direction, so a future drilling well can be placed and oriented optimally in the field. For example, in ultralow permeability shale or sandstone formations that require hydrau-

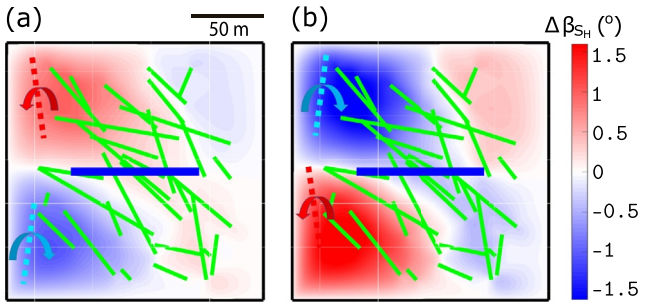

Figure 8. Change in direction, β_{S_H} (degrees), of the maximum horizontal stress S_H, measured from its initial direction along the y-axis. A positive angle means the principal stress rotates counter-clockwise while a negative angle indicates clockwise rotation. The dashed lines indicate the new S_H direction, which is different in different compartments. Green thick lines are the embedded fracture network. The thick blue line is the well trajectory. Two time steps are shown: (a) at the end of injection and (b) at the end of withdrawal.

lic fracturing to boost wellbore injectivity/productivity, the objective is to align the well along the minimum principal stress direction, so that the fractures orthogonal to the wellbore can open up easily against the minimum compression. In these scenarios, a rigid approach to drilling wells without any consideration to the dynamically evolving stress field is guaranteed to yield unfavorable stress-alignment conditions and sub-optimal performance of the wells. Figure 8 shows the rotation angle $\Delta\beta_{S_H}$ of the maximum principal stress S_H, describing a reorientation of the local principal stress field. We observe regions on the two sides of the well with opposite changes in the stress orientation (red and blue shades), and we observe larger changes of $\Delta\beta_{S_H}$ near the left boundary compared to those near the right boundary (lighter shades). This can be explained by the contribution of anisotropic fracture network orientation (predominantly oriented Northwest-Southeast) to the non-uniform movement of tracer, perturbing the pressure field correspondingly. More tracer invasion in the Northwest (NW) and Southeast (SE) corners leads to a pore fluid mixture of lower viscosity and less pressure drop away from the injection well (Figure 5). This results in the reorientation of S_H in the NW-SE regions to be more aligned with the predominant fracture orientation, coinciding with the direction of the slowest change of pore fluid pressure. In addition, fluid-solid poroelastic coupling results in the occurrence of small shear stress perturbation (which is also observed in Figures 16 and 17) during injection, further augmenting the reorientation of principal stresses locally.

6.1.3. Effect of Flow Properties on Fracture Dynamics and Stress Coupling

Based on the prescribed initial stress field and fracture orientations, an initial distribution of fracture permeabilities in the domain is calculated using empirical correlations from Barton et al. (1985). In the initialization step, fracture orientation contributes to the fracture permeability distribution, which is shown by the black line with the square marker in Figure 9. Depending on how favorable a fracture's orientation is to the anisotropic stress field due to the applied boundary condition, each fracture segment responds differently to the stress field. The empirical cumulative distribution function (ECDF) of the fracture permeability is shown in Figure 9 at selected time steps. In our method, each fracture is composed of multiple fracture sub-segments that experience different stress states based on the stress states of the matrix nodes surrounding a sub-segment. This generates assorted permeability changes for the segments. When injection starts, besides the aperture opening due to decreasing effective compression, shear-induced dilation causes additional opening of fracture aperture (Asadollahi & Tonon, 2010). Therefore, the rich complexity of the stress field explains the spatial heterogeneity of fracture permeability despite the tight range of reference starting values (Figure 9). Because of the reduction in normal effective stress and the effect of shear-induced dilation, the fracture permeability values during the injection period (curve with the star marker) is approximately 17% higher compared to those during the withdrawal period (curve with the diamond marker). During injection, shear stress accumulates until shear slip is activated on a particular fracture sub-segment based on the Mohr-Coulomb failure criterion (i.e., fracture shear stress exceeds the product of fracture effective normal stress and the static frictional coefficient $\tau^f \geq \mu_s \sigma_n'^f$). The shear-induced dilation effect during injection is larger on fractures with higher post-initialization values of k^f. Therefore, the spread of permeability range is amplified in the injection period compared to the withdrawal period.

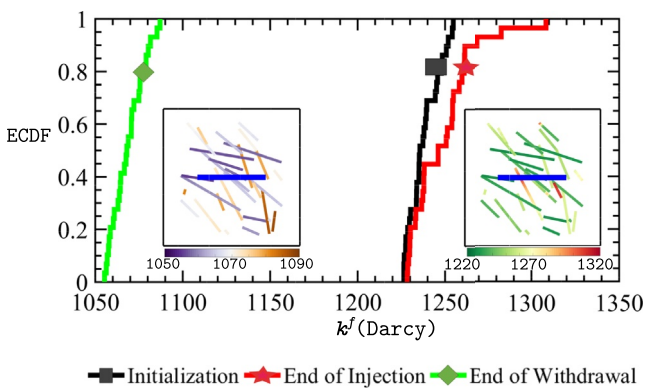

Figure 9. Empirical cumulative distribution function (ECDF) of the fracture permeability k^f after initialization (square marker), at the end of injection (star marker), and at the end of withdrawal (diamond marker). Fracture permeabilities increase during injection and decrease during withdrawal. The two inset figures show the spatial distributions of k^f at the respective timesteps: injection in the right inset and withdrawal in the left inset. The insets use different color scales to highlight the different fractures activated during different episodes–injection and withdrawal.

The temporal evolution of fracture permeability is governed by both fracture orientation and excess effective normal stress acting on the fracture surfaces (Figure 10). On panel (a) of Figure 10, three representative fractures are chosen from the segments that slipped during the course

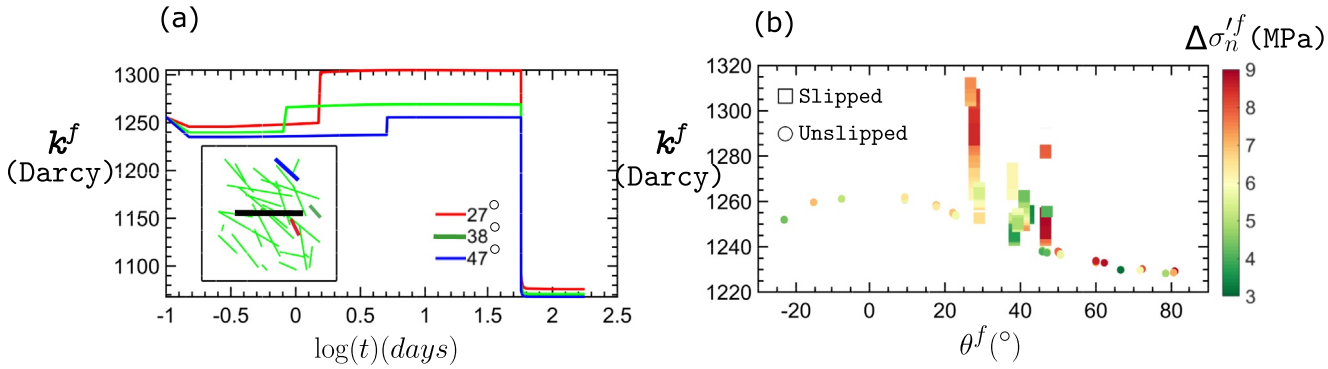

Figure 10. The temporal evolution of fracture permeability and its dependence on fracture orientation θ^f. The fracture orientation θ^f (degrees) is defined as the angle between the fracture plane and the initial S_H direction (i.e., true North). It ranges from – 90° (clockwise from true North) to 90° (counter-clockwise from true North). The true North is the direction of S_H in Figure 1. Panel (a) plots the permeability of three representative fracture segments that slipped and experienced shear-induced dilation during the injection period. The legend shows different orientations of each fracture segments. The horizontal time axis is plotted on a log scale to illustrate the early injection period better. The mini-panel shows the locations of the fracture segments that are plotted. Panel (b) plots fracture permeability and orientation for all fracture segments. The circle markers represent unslipped segments and square markers denote slipped segments. The points are color-coded by the absolute magnitude of excess normal effective stress acting on the fracture segments $\Delta\sigma_n'^f$.

of injection. All fractures start with a constant and prescribed value of k^f that changes during the model initialization step discussed above, which appears as the first drop in k^f (Figure 10a). Then, during the injection period, before any shear slip occurs, k^f increases very slowly because the effective normal compression decreases slowly. The permeability trend exhibits an abrupt jump due to a shear slip event with the timing and magnitude of the event depending on the fracture orientation and the stress state. Fractures that are more favorably aligned (or quasi-parallel to the vertical S_H, i.e., smaller θ^f) experience a larger increase in their stress-dependent permeability because their apertures open up against the minimum horizontal principal stress S_h. The larger the angle, the smaller the fracture opening is due to increasing effective normal stress and a smaller shear-induced dilation. As a result, the evolution of k^f can be split into two periods with the corresponding mechanisms: the inter-slip period when the effective normal stress dictates k^f and the co-slip period when the shear slip dictates k^f. Interestingly, these shear slip events can be physically connected to microseismic episodes, if additional related studies are pursued. Finally, a sharp drop of fracture permeability between injection and withdrawal is expected owing to the sign reversal of the excess pore pressure. To increase the confidence in our fracture dynamics model, the quantitative trends of fracture permeability versus stress magnitude, stress history, and slip displacement are checked against existing literature (Lamur et al., 2017; Watanabe et al., 2008). As observed in panel (b) of Figure 10, only a narrow range of fracture orientation experience shear slip (between 25° and 50°). Slipped segments show higher permeability change compared to unslipped segments mainly due to the shear-induced dilation effect. Among the slipped segments, permeability change is highest for fractures of lower orientation angles (≈ 25 – 30°) and higher values of the excess effective normal stress $\Delta\sigma_n'^f$ (denoted as red filled squares in Figure 10b).

Table 4
Sensitivity Parameter Values

Parameter	Low · base · high	Unit
Biot coefficient α	0.2 · 0.5 · 0.9	
Fluid compressibility C_f	0.4 · 0.5 · 1	GPa^{-1}
Log viscosity ratio R	0 · 2 · 2.5	
Young Modulus E	10 · 25.55 · 50	MPa
Joint compressive strength	120 · 130 · 150	MPa
Joint roughness coefficient	8 · 8 · 20	
Diffusion coefficient D_d	$2\times10^{-8}\cdot2\times10^{-7}\cdot2\times10^{-5}$	m^2s^{-1}

7. Sensitivity Analysis

To better understand the coupling mechanisms between transport and deformation processes in an aquifer, whose properties can vary over a wide and/or uncertain range, we perform a sensitivity analysis to investigate the influence of key rock-fluid properties on different outputs of the Base Case defined above. As the outputs of the coupled simulation can be classified into flow (e.g., pressure), transport (e.g., degree of mixing), and geomechanics (e.g., stresses) categories, so the rock-fluid properties can also be classified into the corresponding categories that control the flow-geomechanics coupling strength (Biot coefficient α, fluid compressibility C_f, rock's Young modulus E), flow-transport coupling strength (log vis-

cosity ratio R, diffusion coefficient D_d), and geomechanics-fracture mechanics coupling strength (JRC, JCS). Table 4 lists the range of investigation of these sensitivity parameters. The base case values are in the middle of the sensitivity range except for JRC, because JRC is empirically constrained by the original Bandis model based on the magnitude of in-situ stresses, which also narrows the sensitivity range of JCS.

7.1. Poroelasticity and Fracture Dynamics Affect Mixing and Spreading

Here, we investigate how different types of coupling lead to changes in the solute transport behavior. Spreading and mixing are critical transport phenomena, which can be quantified using the tracer breakthrough time t_{BT} and the domain-averaged degree of mixing at breakthrough, ζ_{BT} (Jha et al., 2011a, 2011b, 2013; Tran & Jha, 2020). The degree of mixing ζ can be defined in terms of the matrix concentration field:

$$\zeta(t) = 4\overline{(c^m \phi_d \phi_d (1 - c^m))}, \tag{31}$$

where $\phi_d = \phi/\phi_0$ and the overbar indicates volume averaging. ζ ranges from 0 to 1, with $\zeta = 0$ representing an unmixed state and $\zeta = 1$ representing a completely mixed state between injectant and resident fluids. The tornado plot in Figure 11 shows the range of magnitude change (in percentage) of t_{BT} and ζ_{BT}, compared to the base case, for all sensitivity parameters. We observe different levels of impact on t_{BT} and ζ_{BT} for parameters belonging to different types of the coupling mechanism. For all cases except in one scenario, we observe a monotonous relation between each sensitivity parameter listed in Table 4 and the macroscopic transport metrics t_{BT} and ζ_{BT}. There exists a non-monotonous trend in the relationship between Biot coefficient α and t_{BT}, which means tracer breakthrough is fastest in a moderately consolidated reservoir. This nonlinearity may partly stem from the quadratic relationship between α and the incremental porosity change $\delta\phi^m$ expressed in Equation 15. For an incompressible system, or in the drained deformation case, the Biot coefficient can be interpreted as the change in porosity for a unit change in the volumetric strain (Tran & Jha, 2020). This phenomenon is also likely because α is present in both the fluid mass balance equation and the mechanics linear momentum balance equation, which complicates its effect on the pressure field and results in a nonlinear relationship with the transport metrics. For the range of α we examined (from 0.2 to 0.9), changes in t_{BT} and ζ_{BT} are apparently small (approximately 6%) but could be significant for a real site where the absolute breakthrough time is in the order of months, meaning a 6% error margin could translate into an error in the estimated t_{BT} of the order of a week. In those cases, it will be costly to ignore the coupling in the model. Besides, here, the degree of mixing is taken to be the average value for the whole

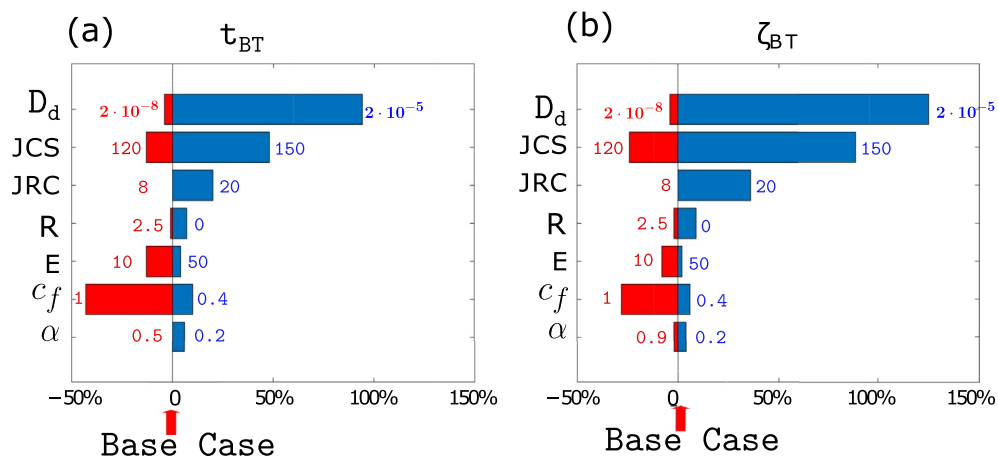

Figure 11. Tornado plot of the percentage change of breakthrough time t_{BT} (panel [a]) and degree of mixing ζ_{BT} (panel [b]) compared to the base case of different sensitivity parameters listed on the y-axis. From bottom to top on the vertical axis: Biot Coefficient α, Fluid Compressibility c_f, Young Modulus E, Log Viscosity Ratio R, joint roughness coefficient, joint compressive strength, Diffusion Coefficient D_d. Red columns to the left show reduction while blue columns to the right show increase of either the breakthrough time or the degree of mixing compared to the base case. The two values on the two ends of each sensitivity bar indicate the corresponding values of each sensitivity parameter, with units shown in Table 4.

domain, which may provide only low resolution information in a fractured aquifer where tracer generally accumulates around the major fractures. We will have a better look at the impact of mechanical coupling on the spatial distribution of the tracer in the next section.

Regarding the fluid compressibility, higher C_f (more compressible fluid, weaker flow-geomechanical coupling) leads to a faster breakthrough (Figure 11). Higher C_f leads to lower Biot modulus and higher values of the pressure time derivative, that is, the fluid accumulation term. The Darcy velocity increases, especially in high permeability channels, which effectively reduces t_{BT}. Regarding rock's modulus, lower E (softer rock, stronger flow-geomechanical coupling) leads to a faster breakthrough of the tracer. Compared to flow-geomechanics coupling parameters (C_f and E), fracture dynamics parameters (JRC, JCS) have a larger impact on transport: tracer breakthrough is retarded (t_{BT} increases) and the fluid mixing is enhanced (ζ_{BT} increases). This impact is physically intuitive in a fracture-dominated flow setting with a large permeability contrast between fracture and matrix (here the ratio is approximately 2×10^5). Less smooth fracture surfaces (i.e., higher JRC) and less weathered joints (i.e., higher JCS) result in a slower breakthrough, mainly as a consequence of lower fracture permeability from less shear-induced dilation. Interestingly, we find out that joint strength due to weathering exerts a more prominent impact than joint asperity on the macroscopic transport behavior in fractured rocks. Flow-transport coupling strength parameter R plays a less impactful role in controlling the variation of t_{BT} and ζ_{BT} because of its limited presence in the mathematical model of the coupled problem; see concentration-dependent viscosity Equation 18. The diffusion coefficient D_d, which is varying over three orders of magnitudes, has the most significant impact on the transport behavior. A more diffusive tracer propagates slower in the fractures, breaks through later, and creates a longer mixing zone as the tracer diffuses across matrix-fracture interfaces and spreads through the aquifer. We observe a positive correlation between t_{BT} and ζ_{BT} because the longer the tracer stays in the domain before the breakthrough, the longer is the contact duration between the tracer and in-situ fluids, which enhances mixing.

We further probe the effect of poroelastic coupling on transport metrics in terms of spatial distributions of the tracer cloud. In practical applications, there are several stress-altering processes such as drilling of a well, hydraulic fracturing, re-fracturing of a fractured well, fluid injection or production, heat injection or production during geothermal operations and steam injection, and natural or anthropogenic seismicity. The in-situ natural fracture network may also evolve (opening or healing of fractures) due to geochemical processes involving mineral dissolution and precipitation, which adds extra complexities to the evolution of the stress field. As we have shown, consideration of different degrees of geomechanical coupling strength is going to impact the extent of the injectant mixing zone as well as how fast the injectant breaks through at neighboring wells. The extent of the mixing zone and the degree of mixing between the tracer and in-situ fluids determine the efficiency of the injection operation and the quality of model calibration in tracer surveillance studies. In fractured aquifers, when the tracer breaks through at a well, changing the extent or degree of mixing becomes challenging because of the creation of a persistent pathway between the injection and pumping wells. Thus, a common objective in many operations is to maximize the degree of mixing or extend the mixing zone before any breakthrough occurs. Figure 12 illustrates how the Biot coefficient, which is a proxy for the degree of consolidation of the rock and also indicates the strength of flow-geomechanical coupling, modulates tracer distribution in the domain. When the aquifer is more consolidated, either naturally or becomes consolidated over time due to production-induced stresses, we observe a reduction of tracer concentration of up to 35% in the central mixing zone around the injector and along major fracture-matrix interfaces. 35% could be significant considering the cost of tracer injection. This observation supports the need to include proper geomechanical coupling while modeling transport in deformable aquifers.

Next, we revisit the behavior of the tracer retrieval curve and study how it is regulated by not only the fracture morphology (Figure 6) but also the strength of flow-geomechanical coupling represented by E and C_f (Figure 13). The actual field data is restricted to the tracer withdrawal period and is made dimensionless by normalizing the well concentration values with the peak concentration to allow comparison with our solution. More compressible fluid and more compressible rock suppress the peak of the tracer retrieval curve. After the peak, the decreasing slope portion of the curve (Figure 13) is modulated mainly by the fracture morphology (fracture density and orientation), because the flow-geomechanical coupling parameters (E and C_f) have a minor impact on the slope. These effects can provide critical guidance during the calibra-

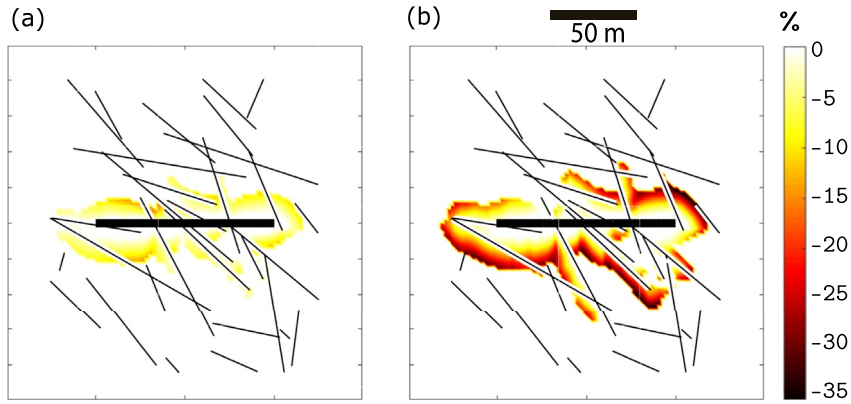

Figure 12. Effect of Biot coefficient α on the tracer concentration distribution. The thick horizontal line is the cyclic well and the thin black lines are the fracture planes. Difference between two concentration fields for (a) $\alpha = 0.5$ and $\alpha = 0.2$ and (b) $\alpha = 0.9$ and $\alpha = 0.2$ are shown at the breakthrough time. The loss of tracer concentration is intensified as the flow-geomechanical coupling strength increases with increasing α.

tion of the aquifer model via tracer retrieval data. The middle section of the well, with a denser and more favorably oriented fracture set, records lower values of the tracer peak concentration due to faster drainage of the tracer. For the ranges used in this sensitivity study, C_f induces a larger relative change to the tracer peak than E.

It is important to note that matching the simulated tracer profile to the observed profile is not the goal here. Instead, our emphasis is on understanding how different coupling parameters regulate the shape of the tracer retrieval curve. In practice, this understanding can be used to improve the qualitative agreement

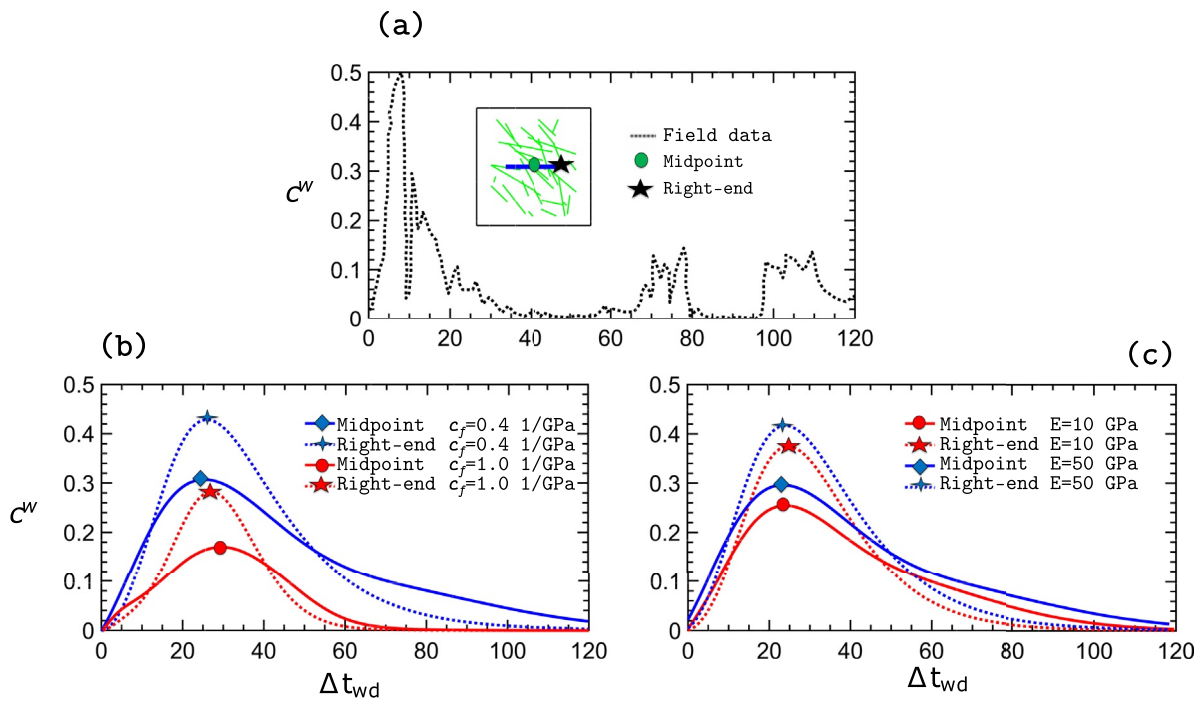

Figure 13. (a) Tracer retrieval curve data from a case study (J. Li et al., 2016). The inset figure shows the location of the well (thick blue line), fracture (thinner green lines), and tracer monitoring stations (midpoint of well and midpoint of the right well segment). The horizontal axis is the time elapsed from the start of the withdrawal period, Δt_{wd}, in days. Panels (b and c) show tracer retrieval curves during tracer withdrawal periods at different well locations for different values of the (b) fluid compressibility C_f and (c) rock Modulus E. Lower panels demonstrate the effect of flow-geomechanical coupling (different colors but same line styles) and fracture morphology (same colors but different line styles). All curves are shifted toward a common starting point on the horizontal axis for better visual comparison.

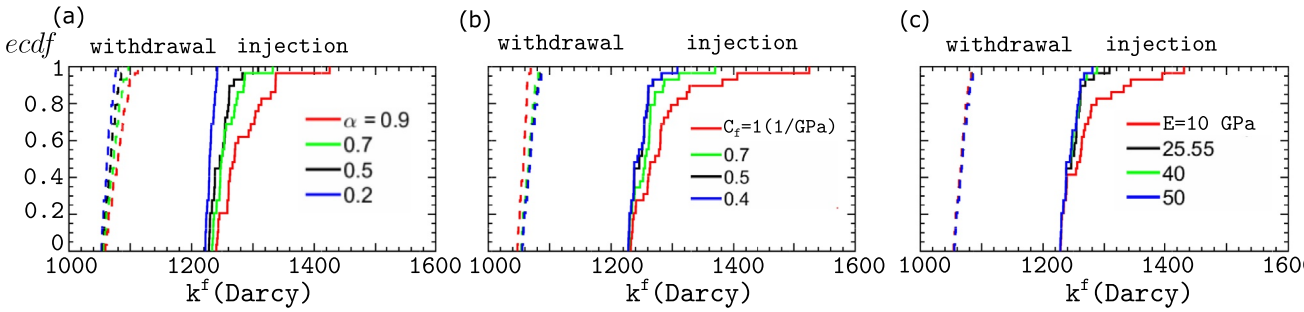

Figure 14. Empirical cumulative distribution function (ECDF) of fracture permeability (k^f) plotted for different values of the (a) Biot coefficient α, (b) fluid compressibility C_f, and (c) rock's modulus E. Injection and withdrawal responses are separated by plotting them as solid and dash lines, respectively.

between modeled and observed tracer curves in terms of their peak concentration and slope values. We examine the effect of fluid compressibility and rock stiffness on the temporal evolution of the degree of mixing (see Figure S3 in Supporting Information S1). These observations suggest that the classical definition of the flow-geomechanics coupling strength parameter (Armero & Simo, 1992; Tran & Jha, 2020), $\eta = \frac{\alpha^2 M}{K_{dr}} = \frac{\alpha^2}{(1-\alpha)(\alpha-\phi)+\phi C_f K_{dr}}$ cannot properly quantify the strength of transport-geomechanics coupling in fractured porous media. This is because macroscopic transport metrics exhibit a nonlinear relationship with α. Also, different trends of ζ_{BT} and t_{BT} are observed if we increase η by the same amount by changing different parameters in its definition. For example, decreasing C_f retards tracer breakthrough and decreasing E accelerates tracer breakthrough, although both lead to increasing η (Figure 11).

Next, we make a deeper investigation into the effect of poroelastic coupling on fracture permeability via stress field because of the critical importance of fracture permeability in dictating flow and transport behavior in fractured porous media. Here, the effect of poroelastic coupling on the synergy between fracture dynamics and transport is demonstrated through the fracture permeability (k^f) evolution during tracer injection and withdrawal (Figure 14). For the sensitivity range of input parameters used, we observe a larger separation of permeability trends in the injection compared to the withdrawal period, mainly because of the shear-induced dilation effect during injection. By the end of the withdrawal period, E shows minimal impact on fracture permeability while C_f and α sensitivity yield approximately 5% change in k^f. In comparison, across the same range of input, by the end of the injection period or tracer breakthrough, E and α contribute to about 16% variation while C_f yields about 25% difference in k^f. Rock that is more unconsolidated (higher α) and softer (lower E) elevates the high end of the permeability range while less compressible pore fluid (lower C_f) inhibits fracture permeability growth. The augmentation of fracture permeability at higher α, higher C_f, and lower E explains the decrease in the tracer breakthrough time for these cases in Figure 11. Another factor that could be considered is the compliance contrast between the fractures and the host matrix. Fractures are often mechanically more compliant than the host rock. Thus, we perform a sensitivity study where the bulk modulus of fractures is lower than that of the matrix (Murdoch & Germanovich, 2006). Please refer to Text S4 and Figures S4–S7 in Supporting Information S1 for the result of fracture compliance study.

7.2. Fingering and Fracturing Parameters Impact the Stress State

We examine and characterize the impact of flow-transport and transport-geomechanics coupling on the state of stress. This understanding is critical to improve the operational design of a cyclic injection/withdrawal operation, for example, to maintain the mechanical integrity of the formation and to avoid reactivation of natural fractures. Here, we specifically focus on the effect of fracture dynamics and transport parameters on geomechanical quantities. While flow-geomechanics coupling has a more significant first-order impact on the stress state, flow-transport coupling through R (i.e., viscous fingering) also exerts considerable influence on the stress field as shown in Figure 15. The effect of fingering is more evident toward the end of the injection period when the tracer has invaded parts of the matrix (bottom panels of Figure 15). In case of no coupling from transport to flow, that is, $R = 0$, we observe a flat trend line signifying there is no dy-

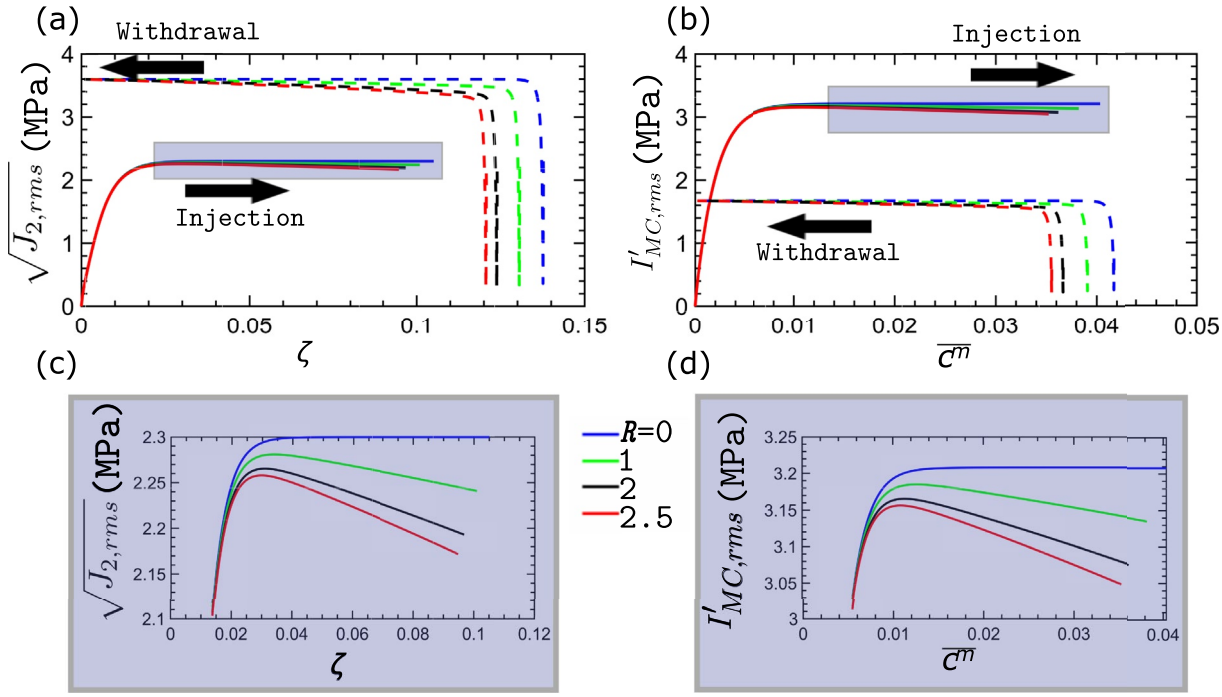

Figure 15. Effect of the log viscosity ratio R, a transport parameter, on the stress state. (a) The root mean square of the square root of the second invariant of deviatoric stress tensor $\sqrt{J_{2,rms}}$ is plotted against the degree of mixing ζ. (b) The root mean square of Mohr-Coulomb stress invariant $I'_{MC,rms}$ is plotted against the domain-averaged concentration $\overline{c^m}$. Evolution during the injection and withdrawal periods are shown via solid and dotted lines, respectively. The direction of time for each period is shown via arrows. The shaded regions are magnified in (c and d) for better visualization.

namic synergy between geomechanics and transport. As R increases, curves between the root mean square (rms) of stress invariants ($I'_{MC,rms}$ and $\sqrt{J_{2,rms}}$) and the transport metrics deviate downward, compared to the $R = 0$ case. For either cases, the discrepancy between $R = 0$ and $R = 2.5$ can amount up to 7% for $\sqrt{J_{2,rms}}$ and 5% for $I'_{MC,rms}$. This emphasizes the need for properly considering this flow-transport coupling mechanism, especially in critically stressed rocks close to failure. Near the injection well, where a significant fraction of the tracer is present and the flow-transport coupling (viscous fingering) dominates, we observe lower values of the Mohr-Coulomb failure function. This suggests that shear failure is less likely to happen in regions with stronger flow-transport coupling.

During the withdrawal period (dashed curves in Figure 15), different R curves start from different points near the bottom right corner of the plot. This horizontal offset between different curves for different R is due to the difference in the degree of mixing (ζ) and the average matrix concentration ($\overline{c^m}$) at the start of the withdrawal period. Toward the end of the withdrawal period, the $R = 0$ curve flattens out, again suggesting negligible dependency between stress and transport parameters. However, with the advent of fingering at $R > 0$, the curves deviate as they did during injection, and the impact of flow-transport coupling on the stress state becomes noticeable. We believe that the dependency of the stress state on transport metrics becomes stronger as the transport controlling parameter increases in value. We also believe that the above observation will hold true if viscous fingering is substituted with density-driven convective instability, which is commonly encountered during seawater intrusion into coastal aquifers (Huyakorn et al., 1987) and CO_2-brine mixing during carbon sequestration in saline aquifers (Metz et al., 2005). In that case, the Rayleigh-Benard or Rayleigh-Taylor instability may substitute the Saffman-Taylor instability, and the density contrast will substitute the viscosity contrast.

Finally, we look at how fracture mechanical properties (joint weathering and joint strength) influence the stability of fractures during injection and withdrawal (Figures 16 and 17). Because JCS and JRC values for an aquifer can be estimated from load testing experiments on core samples, our findings can be used to decide where and how the tracer should be injected to ensure the mechanical integrity of the subsurface. In

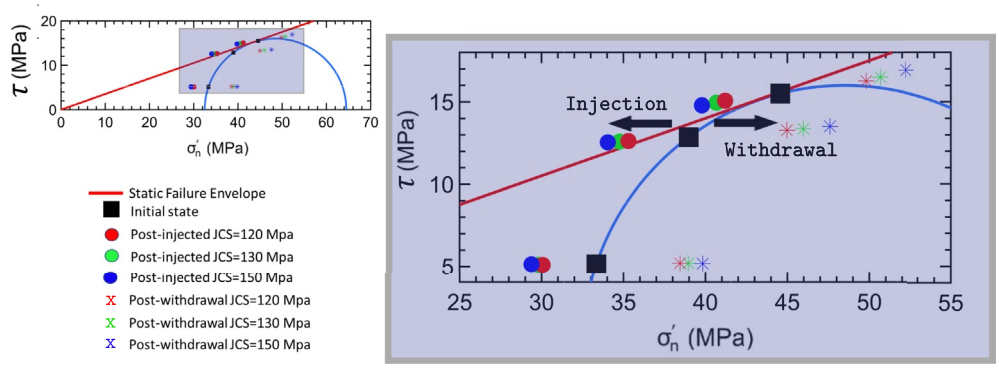

Figure 16. Evolution in the stress states (shear stress τ vs. effective normal stress σ_n') of three representative fracture segments is shown using a Mohr circle diagram. Three timesteps are shown–initial (black square), end of injection (solid circles), and end of withdrawal (asterisks)–for three different JCS values. The static failure envelope is plotted in red with the static frictional coefficient of 0.35. The shaded region in the top left diagram is shown in the right diagram with a zoom-in. The arrows indicate the direction of change in the stress, from the initial state, during injection and withdrawal.

Figures 16 and 17, the effective normal and shear stresses on a selected few fracture segments are plotted on the Mohr diagram to show their evolution with time and fracture properties. In a strike-slip faulting regime (i.e., $S_h < S_v < S_H$ where S_v is the vertical principal stress), the difference between S_h and S_H determines the largest Mohr circle radius. Initially, in absence of any pore pressure perturbation, the initial stresses inside the domain balance the tectonic compressions on the boundary, which can be used to draw the initial Mohr circle. The initial stress states of the fracture segments (denoted by black squares in Figures 16 and 17) lie on the initial Mohr circle. The three squares are at different locations on the circle due to the difference in the fracture orientation. During injection, the normal effective compression σ_n' acting on the fracture segments decreases, which causes the points to move left toward the static frictional failure envelope. Minor movement along the shear stress axis is also observed because the injection-induced expansion of the aquifer applies shear traction on some fractures, the magnitude of which depends on their orientation. In the figure, some points cross the failure envelope because our fracture mechanics model is one-way coupled to the domain equilibrium (Section 3.5) and does not impose a strong restriction on such crossings. The magnitude of change in the stress state determines the likelihood of slip on the fracture. The amount of shift varies depending on the values of fracture mechanics parameters, JRC and JCS. In a reservoir with over-pressured pore fluid or more pronounced stress heterogeneity, these 4–5 MPa stress changes could easily induce slip on fractures. In Figure 16, fractures with higher JCS, implying less weathered joints, have larger stress changes and thus are more likely to fail in the shear mode. During tracer withdrawal, the less

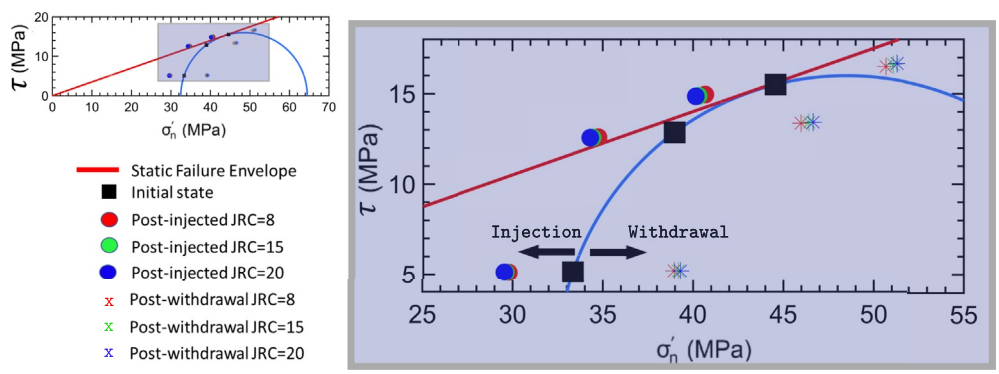

Figure 17. Stress states of three representative fracture segments are plotted in a Mohr diagram at different times: initial (black square), end of injection (solid circles), and end of withdrawal (asterisks) for different JRC values. The static failure envelope is plotted in red with the static frictional coefficient of 0.35. The shaded region in the top left diagram is shown in the right diagram with a zoom-in. The arrows indicate the directional change of stress state from the initial state during injection and withdrawal.

weathered fractures move farther away from the failure envelope, suggesting that they are less likely to slip during this period. For fractures of different JRC, that is, different resistances to shear slip, the magnitude of poroelastic stress shifts are equally pronounced although the sensitivity spread of stress output among JRC values investigated is smaller than that of JCS (Figure 17). This suggests that, compared to the compressive strength, the resistance to shear has a less pronounced effect in governing fracture stability. Fractures with smaller JRC tend to move closer to the failure envelope during injection and farther during withdrawal. This implies that a fracture with lower shear strength is more likely to fail during injection.

8. Conclusions

We proposed a novel multiphysics modeling framework to investigate the rich physical interchange between flow, geomechanics, transport, and fracture dynamics in naturally fractured aquifers. We show that successful integration of transport-geomechanical coupling in field-scale modeling studies of flow through fractured rocks can improve the prediction of macroscopic transport parameters: the tracer breakthrough time, the average and maximum concentrations of the tracer at a control plane, and the evolution of the degree of mixing with time. Additional contributions of the study are as follows:

1. We utilized Embedded Discrete Fracture Modeling (EDFM) to model the fractured porous media and implemented an improved Bandis model to simulate fracture mechanics. Our EDFM-based framework allows modeling multiple randomly oriented intersecting fractures at a lower computational cost than many discrete fracture methods that require a conforming mesh.
2. We characterized the effect of geomechanical coupling on key transport metrics and quantified the impact of each coupling parameter on tracer breakthrough and degree of mixing. We find that parameters governing the fracture dynamics (JCS and JRC) have a higher impact on the spreading and mixing of tracer compared to parameters dictating the strength of flow-geomechanical coupling (Biot coefficient, fluid compressibility, rock's bulk modulus).
3. Tracer retrieval curve characteristics, for example, the peak concentration, are modulated by both fracture morphology and the strength of geomechanical coupling.
4. Flow-transport coupling, via viscous fingering and fracture dynamics, alter the stress state and fracture stability in the domain. This is important to consider in critically stressed formations close to failure.
5. We quantified the impact of flow-geomechanics coupling strength on the evolution of fracture permeability.

Our results suggest that the coupling between flow, transport, and geomechanics will be necessary to accurately model the fate of an active tracer (which dynamically modifies the viscosity or density of the flow) during reservoir surveillance, contaminant remediation, or fracture characterization studies in deformable rocks. For shallower reservoirs (for example, in groundwater applications), we hypothesize that the coupling between geomechanics and transport can become stronger when the rock is more stress-sensitive due to a lower degree of consolidation (higher Biot coefficient) and lower bulk modulus. The findings of this study could help motivate and inform the future design and deployment of sensors that can monitor small ($< 10\%$) changes in stress/strain fields that may arise from coupling with the flow and transport processes. An example of such high fidelity and precision measurement technique is Distributed Strain Sensing (DSS), which uses fiber optics technology to reliably detect small changes in stress/strain fields around a wellbore.

Our modeling framework assumes that the feedback from fracture slip to the matrix stress is via changes in fracture properties only. We neglect fracture slip-induced stress relaxation, which can become important in case of fractures/faults that rupture over a long distance or grow in length from their tips. A future extension of our work includes modeling the propagation and healing of fractures to capture the feedback from fracture deformation to stress. Extending the framework to enable the generation of synthetic microseismic events can also create new possibilities for assimilating microseismic monitoring data and calibrating the proposed multiphysics model. Finally, the proposed modeling framework can support multiphysics joint inversion endeavors (Jha et al., 2015) at monitoring sites with multiphysics data from InSAR/GPS satellites, ground penetrating radar, and wells to estimate uncertain hydraulic and poroelastic properties of the subsurface.

Data Availability Statement

Data set for Figure 13 panel (a) is available in J. Li et al. (2016). No other data is used in the study. Copyright permission to reuse Figure 2 is obtained from the Society of Petroleum Engineers (SPE).

Acknowledgment
This research was partially supported by funding from a project funded by the US National Science Foundation Hydrologic Sciences Program (Number 2025285).

References

Abousleiman, Y., Cheng, A.-D., Cui, L., Detournay, E., & Roegiers, J.-C. (1996). Mandel's problem revisited. *Géotechnique*, *46*(2), 187–195. https://doi.org/10.1680/geot.1996.46.2.187

Armero, F., & Simo, J. C. (1992). A new unconditionally stable fractional step method for non-linear coupled thermomechanical problems. *International Journal for Numerical Methods in Engineering*, *35*(4), 737–766. https://doi.org/10.1002/nme.1620350408

Asadollahi, P., & Tonon, F. (2010). Constitutive model for rock fractures: Revisiting Barton's empirical model. *Engineering Geology*, *113*(1–4), 11–32. https://doi.org/10.1016/j.enggeo.2010.01.007

Bandis, S., Lumsden, A., & Barton, N. (1983). Fundamentals of rock joint deformation. *International Journal of Rock Mechanics and Mining Sciences & Geomechanics Abstracts*, *20*, 249–268. https://doi.org/10.1016/0148-9062(83)90595-8

Barton, N. (1982). *Modelling rock joint behavior from in situ block tests: Implications for nuclear waste repository design* (Vol. 308). Office of Nuclear Waste Isolation, Battelle Project Management Division.

Barton, N., Bandis, S., & Bakhtar, K. (1985). Strength, deformation and conductivity coupling of rock joints. *International Journal of Rock Mechanics and Mining Sciences & Geomechanics Abstracts*, *22*, 121–140. https://doi.org/10.1016/0148-9062(85)93227-9

Barton, N., & Choubey, V. (1977). The shear strength of rock joints in theory and practice. *Rock Mechanics*, *10*, 1–54. https://doi.org/10.1007/bf01261801

Bonazzi, A., Jha, B., & de, Barros, F. P. J. (2020). Transport analysis in deformable porous media through integral transforms. *International Journal for Numerical and Analytical Methods in Geomechanics*, *45*, 1–324. https://doi.org/10.1002/nag.3150

Bonazzi, A., Morvillo, M., Im, J., Jha, B., & de, Barros, F. P. J. (2021). Relative impacts of permeability heterogeneity and viscosity contrast on solute mixing. *Physical Review Fluids*, *6*, 064501. https://doi.org/10.1103/PhysRevFluids.6.064501

Borja, R. I. (2013). *Plasticity: Modeling & computation*. Springer Science & Business Media.

Bubshait, A., & Jha, B. (2019). Coupled poromechanics-damage mechanics modeling of fracturing during injection in brittle rocks. *International Journal for Numerical Methods in Engineering*, *121*, 256–276. https://doi.org/10.1002/nme.6208

Castelletto, N., White, J. A., & Tchelepi, H. (2015). Accuracy and convergence properties of the fixed-stress iterative solution of two-way coupled poromechanics. *International Journal for Numerical and Analytical Methods in Geomechanics*, *39*(14), 1593–1618. https://doi.org/10.1002/nag.2400

Chai, Z., Tang, H., He, Y., Killough, J., & Wang, Y. (2018). Uncertainty quantification of the fracture network with a novel fractured reservoir forward model. In *SPE annual technical conference and exhibition*. OnePetro. https://doi.org/10.2118/191395-ms

Cirpka, O. A., & Valocchi, A. J. (2007). Two-dimensional concentration distribution for mixing-controlled bioreactive transport in steady state. *Advances in Water Resources*, *30*(6–7), 1668–1679. https://doi.org/10.1016/j.advwatres.2006.05.022

Cornaton, F. J., Park, Y. J., Normani, S. D., Sudicky, E. A., & Sykes, J. F. (2008). Use of groundwater lifetime expectancy for the performance assessment of a deep geologic waste repository: 1. Theory, illustrations, and implications. *Water Resources Research*, *44*. https://doi.org/10.1029/2007WR006208

Coussy, O. (2004). *Poromechanics*. John Wiley & Sons.

Dentz, M., Le Borgne, T., Englert, A., & Bijeljic, B. (2011). Mixing, spreading and reaction in heterogeneous media: A brief review. *Journal of Contaminant Hydrology*, *120*, 1–17. https://doi.org/10.1016/j.jconhyd.2010.05.002

Flowers, T. C., & Hunt, J. R. (2007). Viscous and gravitational contributions to mixing during vertical brine transport in water-saturated porous media. *Water Resources Research*, *43*(1). https://doi.org/10.1029/2005wr004773

Fox, P. J., Lee, J., & Lenhart, J. J. (2011). Coupled consolidation and contaminant transport in compressible porous media. *International Journal of Geomechanics*, *11*(2), 113–123. https://doi.org/10.1061/(asce)gm.1943-5622.0000035

Guo, X., Wu, K., An, C., Tang, J., & Killough, J. (2019). Numerical investigation of effects of subsequent parent-well injection on interwell fracturing interference using reservoir-geomechanics-fracturing modeling. *SPE Journal*, *24*(4), 1–884. https://doi.org/10.2118/195580-pa

Hajibeygi, H., Karvounis, D., & Jenny, P. (2011). A hierarchical fracture model for the iterative multiscale finite volume method. *Journal of Computational Physics*, *230*(24), 8729–8743. https://doi.org/10.1016/j.jcp.2011.08.021

Hardebol, N. J., Maier, C., Nick, H., Geiger, S., Bertotti, G., & Boro, H. (2015). Multiscale fracture network characterization and impact on flow: A case study on the Latemar carbonate platform. *Journal of Geophysical Research: Solid Earth*, *120*(12), 8197–8222. https://doi.org/10.1002/2015jb011879

Homsy, G. M. (1987). Viscous fingering in porous media. *Annual Review of Fluid Mechanics*, *19*(1), 271–311. https://doi.org/10.1146/annurev.fl.19.010187.001415

Hu, Q., & Moran, J. E. (2005). Simultaneous analyses and applications of multiple fluorobenzoate and halide tracers in hydrologic studies. *Hydrological Processes*, *19*(14), 2671–2687. https://doi.org/10.1002/hyp.5780

Huyakorn, P. S., Andersen, P. F., Mercer, J. W., & White, H. O., Jr. (1987). Saltwater intrusion in aquifers: Development and testing of a three-dimensional finite element model. *Water Resources Research*, *23*, 293–312. https://doi.org/10.1029/WR023i002p00293

Iding, M., & Ringrose, P. (2010). Evaluating the impact of fractures on the performance of the In Salah CO_2 storage site. *International Journal of Greenhouse Gas Control*, *4*(2), 242–248. https://doi.org/10.1016/j.ijggc.2009.10.016

Jansen, G., Valley, B., & Miller, S. A. (2018). *THERMAID - A matlab package for thermo-hydraulic modeling and fracture stability analysis in fractured reservoirs*. arXiv preprint arXiv:1806.10942.

Jha, B., Bottazzi, F., Wojcik, R., Coccia, M., Bechor, N., Mclaughlin, D., & Juanes, R. (2015). Reservoir characterization in an underground gas storage field using joint inversion of flow and geodetic data. *International Journal for Numerical and Analytical Methods in Geomechanics*, *39*, 1619–1638. https://doi.org/10.1002/2013WR015175

Jha, B., Cueto-Felgueroso, L., & Juanes, R. (2011a). Fluid mixing from viscous fingering. *Physical Review Letters*, *106*(19), 194502. https://doi.org/10.1103/physrevlett.106.194502

Jha, B., Cueto-Felgueroso, L., & Juanes, R. (2011b). Quantifying mixing in viscously unstable porous media flows. *Physical Review E*, *84*(6), 066312. https://doi.org/10.1103/physreve.84.066312

Jha, B., Cueto-Felgueroso, L., & Juanes, R. (2013). Synergetic fluid mixing from viscous fingering and alternating injection. *Physical Review Letters*, *111*(14), 144501. https://doi.org/10.1103/physrevlett.111.144501
Jha, B., & Juanes, R. (2007). A locally conservative finite element framework for the simulation of coupled flow and reservoir geomechanics. *Acta Geotech*, *2*, 139–153. https://doi.org/10.1007/s11440-007-0033-0
Jha, B., & Juanes, R. (2014). Coupled multiphase flow and poromechanics: A computational model of pore pressure effects on fault slip and earthquake triggering. *Water Resources Research*, *50*(5), 3776–3808. https://doi.org/10.1002/2013wr015175
Jiménez-Martínez, J., Porter, M. L., Hyman, J. D., Carey, J. W., & Viswanathan, H. S. (2016). Mixing in a three-phase system: Enhanced production of oil-wet reservoirs by CO_2 injection. *Geophysical Research Letters*, *43*, 196–205. https://doi.org/10.1002/2015GL066787
Jin, L., & Zoback, M. D. (2018). Fully dynamic spontaneous rupture due to quasi-static pore pressure and poroelastic effects: An implicit nonlinear computational model of fluid-induced seismic events. *Journal of Geophysical Research: Solid Earth*, *123*, 9430–9468. https://doi.org/10.1029/2018jb015669
Lamur, A., Kendrick, J., Eggertsson, G., Wall, R., Ashworth, J., & Lavallée, Y. (2017). The permeability of fractured rocks in pressurised volcanic and geothermal systems. *Scientific Reports*, *7*(1), 1–9. https://doi.org/10.1038/s41598-017-05460-4
Latham, J.-P., Xiang, J., Belayneh, M., Nick, H. M., Tsang, C.-F., & Blunt, M. J. (2013). Modelling stress-dependent permeability in fractured rock including effects of propagating and bending fractures. *International Journal of Rock Mechanics and Mining Sciences*, *57*, 100–112. https://doi.org/10.1016/j.ijrmms.2012.08.002
Lee, S. H., Lough, M., & Jensen, C. (2001). Hierarchical modeling of flow in naturally fractured formations with multiple length scales. *Water Resources Research*, *37*(3), 443–455. https://doi.org/10.1029/2000wr900340
Levison, J. K., & Novakowski, K. S. (2012). Rapid transport from the surface to wells in fractured rock: A unique infiltration tracer experiment. *Journal of Contaminant Hydrology*, *131*(1), 29–38. https://doi.org/10.1016/j.jconhyd.2012.01.001
Lewis, R. W., & Sukirman, Y. (1993). Finite element modeling for simulating the surface subsidence above a compacting hydrocarbon reservoir. *International Journal for Numerical and Analytical Methods in Geomechanics*, *18*, 619–639.
Li, J., Pei, Y., Jiang, H., Zhao, L., Li, L., Zhou, H., & Zhang, Z. (2016). Tracer flowback based fracture network characterization in hydraulic fracturing. In *Abu Dhabi International Petroleum Exhibition & Conference*. OnePetro. https://doi.org/10.2118/183444-ms
Li, S., Zhang, D., & Li, X. (2017). A new approach to the modeling of hydraulic-fracturing treatments in naturally fractured reservoirs. *SPE Journal*, *22*(4), 1–64. https://doi.org/10.2118/181828-pa
Li, X., Li, X., Zhang, D., & Yu, R. (2020). A dual-grid, implicit, and sequentially coupled geomechanics-and-composition model for fractured reservoir simulation. *SPE Journal*, *25*(4). https://doi.org/10.2118/201210-pa
Matthäi, S. K., Nick, H. M., Pain, C., & Neuweiler, I. (2010). Simulation of solute transport through fractured rock: A higher-order accurate finite-element finite-volume method permitting large time steps. *Transport in Porous Media*, *83*(2), 289–318. https://doi.org/10.1007/s11242-009-9440-z
McCarthy, J., & Zachara, J. (1989). Subsurface transport of contaminants. *Environmental Science & Technology*, *23*(5), 496–502. https://doi.org/10.1021/es00063a001
Meguerdijian, S., & Jha, B. (2021). Quantification of fault leakage dynamics based on leakage magnitude and dip angle. *International Journal for Numerical and Analytical Methods in Geomechanics*. https://doi.org/10.1002/nag.3267
Mercer, J. W., & Cohen, R. M. (1990). A review of immiscible fluids in the subsurface: Properties, models, characterization and remediation. *Journal of Contaminant Hydrology*, *6*(2), 107–163. https://doi.org/10.1016/0169-7722(90)90043-g
Metz, D., Davidson, O., de, Connick, H., Loos, M., & Meyer, L. (2005). *IPCC special report on carbon dioxide capture and storage* (pp. 201–213). Cambridge University Press.
Moinfar, A., Sepehrnoori, K., Johns, R. T., & Varavei, A. (2013). Coupled geomechanics and flow simulation for an embedded discrete fracture model. In *SPE reservoir simulation symposium*. OnePetro. https://doi.org/10.2118/163666-ms
Murdoch, L. C., & Germanovich, L. N. (2006). Analysis of a deformable fracture in permeable material. *International Journal for Numerical and Analytical Methods in Geomechanics*, *30*(6), 529–561. https://doi.org/10.1002/nag.492
Myshakin, E., Siriwardane, H., Hulcher, C., Lindner, E., Sams, N., King, S., & McKoy, M. (2015). Numerical simulations of vertical growth of hydraulic fractures and brine migration in geological formations above the Marcellus shale. *Journal of Natural Gas Science and Engineering*, *27*, 531–544. https://doi.org/10.1016/j.jngse.2015.08.030
Nicolaides, C., Jha, B., Cueto-Felgueroso, L., & Juanes, R. (2015). Impact of viscous fingering and permeability heterogeneity on fluid mixing in porous media. *Water Resources Research*, *51*(4), 2634–2647. https://doi.org/10.1002/2014wr015811
Norbeck, J. H., McClure, M. W., Lo, J. W., & Horne, R. N. (2016). An embedded fracture modeling framework for simulation of hydraulic fracturing and shear stimulation. *Computational Geosciences*, *20*(1), 1–18. https://doi.org/10.1007/s10596-015-9543-2
Olsson, R., & Barton, N. (2001). An improved model for hydromechanical coupling during shearing of rock joints. *International Journal of Rock Mechanics and Mining Sciences*, *38*(3), 317–329. https://doi.org/10.1016/s1365-1609(00)00079-4
Peaceman, D. W. (1978). Interpretation of well-block pressures in numerical reservoir simulation (includes associated paper 6988). *Society of Petroleum Engineers Journal*, *18*(03), 183–194. https://doi.org/10.2118/6893-pa
Pogacnik, J., Elsworth, D., O'Sullivan, M., & O'Sullivan, J. (2016). A damage mechanics approach to the simulation of hydraulic fracturing/shearing around a geothermal injection well. *Computers and Geotechnics*, *71*, 338–351. https://doi.org/10.1016/j.compgeo.2015.10.003
Poulsen, M. M., & Kueper, B. H. (1992). A field experiment to study the behavior of tetrachloroethylene in unsaturated porous media. *Environmental Science & Technology*, *26*, 889–895. https://doi.org/10.1021/es00029a003
Rugh, D., & Burbey, T. (2008). Using saline tracers to evaluate preferential recharge in fractured rocks, Floyd County, Virginia, USA. *Hydrogeology Journal*, *16*, 251–262. https://doi.org/10.1007/s10040-007-0236-3
Rutqvist, J., & Stephansson, O. (2003). The role of hydromechanical coupling in fractured rock engineering. *Hydrogeology Journal*, *11*(1), 7–40. https://doi.org/10.1007/s10040-002-0241-5
Sahimi, M. (2011). *Flow and transport in porous media and fractured rock: From classical methods to modern approaches* (2nd ed.). Wiley–VCH.
Sangnimnuan, A., Li, J., & Wu, K. (2018). Development of efficiently coupled fluid-flow/geomechanics model to predict stress evolution in unconventional reservoirs with complex-fracture geometry. *SPE Journal*, *23*(03), 640–660. https://doi.org/10.2118/189452-pa
Shakiba, M. (2014). *Modeling and simulation of fluid flow in naturally and hydraulically fractured reservoirs using embedded discrete fracture model (EDFM)* (Unpublished doctoral dissertation). University of Texas Austin.
Sweeney, M. R., & Hyman, J. D. (2020). Stress effects on flow and transport in three-dimensional fracture networks. *Journal of Geophysical Research: Solid Earth*, *125*(8), e2020JB019754. https://doi.org/10.1029/2020JB019754
Tene, M., Bosma, S. B., Al Kobaisi, M. S., & Hajibeygi, H. (2017). Projection-based embedded discrete fracture model (pEDFM). *Advances in Water Resources*, *105*, 205–216.

Tran, M., Aminzadeh, F., & Jha, B. (2018). Effect of coupled flow and geomechanics on transport of a fluid slug in a stress-sensitive reservoir. In *52nd US Rock Mechanics/Geomechanics Symposium*. OnePetro.

Tran, M., & Jha, B. (2020). Coupling between transport and geomechanics affects spreading and mixing during viscous fingering in deformable aquifers. *Advances in Water Resources*, *136*, 103485. https://doi.org/10.1016/j.advwatres.2019.103485

Warner, N., Darrah, T., Jackson, R., Millot, R., Kloppmann, W., & Vengosh, A. (2014). New tracers identify hydraulic fracturing fluids and accidental releases from oil and gas operations. *Environmental Science & Technology*, *48*(21), 12552–12560. https://doi.org/10.1021/es5032135

Watanabe, N., Hirano, N., & Tsuchiya, N. (2008). Determination of aperture structure and fluid flow in a rock fracture by high-resolution numerical modeling on the basis of a flow-through experiment under confining pressure. *Water Resources Research*, *44*(6). https://doi.org/10.1029/2006wr005411

Witherspoon, P. A., Cook, N., & Gale, J. (1981). Geologic storage of radioactive waste: Field studies in Sweden. *Science*, *211*(4485), 894–900. https://doi.org/10.1126/science.7466363

Yan, X., Huang, Z., Yao, J., Zhang, Z., Liu, P., Li, Y., & Fan, D. (2019). Numerical simulation of hydro-mechanical coupling in fractured vuggy porous media using the equivalent continuum model and embedded discrete fracture model. *Advances in Water Resources*, *126*, 137–154. https://doi.org/10.1016/j.advwatres.2019.02.013

Ye, Z., & Ghassemi, A. (2018). Injection-induced shear slip and permeability enhancement in granite fractures. *Journal of Geophysical Research: Solid Earth*, *123*(10), 9009–9032. https://doi.org/10.1029/2018jb016045

Zhao, X., & Jha, B. (2019). Role of well operations and multiphase geomechanics in controlling fault stability during CO_2 storage and enhanced oil recovery. *Journal of Geophysical Research: Solid Earth*, *124*, 6359–6375. https://doi.org/10.1029/2019JB017298

Zhao, X., & Jha, B. (2021). A new coupled multiphase flow–finite strain deformation–fault slip framework for induced seismicity. *Journal of Computational Physics*, *433*, 110178. https://doi.org/10.1016/j.jcp.2021.110178

Zhao, Z., Jing, L., Neretnieks, I., & Moreno, L. (2011). Numerical modeling of stress effects on solute transport in fractured rocks. *Computers and Geotechnics*, *38*(2), 113–126. https://doi.org/10.1016/j.compgeo.2010.10.001